REVIEW ARTICLE
https://doi.org/10.1038/s41560-019-0463-6

nature energy

Passivating contacts for crystalline silicon solar cells

Thomas G. Allen[1,4], James Bullock[2,3,4], Xinbo Yang[1], Ali Javey[3] and Stefaan De Wolf[1*]

The global photovoltaic (PV) market is dominated by crystalline silicon (c-Si) based technologies with heavily doped, directly metallized contacts. Recombination of photo-generated electrons and holes at the contact regions is increasingly constraining the power conversion efficiencies of these devices as other performance-limiting energy losses are overcome. To move forward, c-Si PV technologies must implement alternative contacting approaches. Passivating contacts, which incorporate thin films within the contact structure that simultaneously supress recombination and promote charge-carrier selectivity, are a promising next step for the mainstream c-Si PV industry. In this work, we review the fundamental physical processes governing contact formation in c-Si. In doing so we identify the role passivating contacts play in increasing c-Si solar cell efficiencies beyond the limitations imposed by heavy doping and direct metallization. Strategies towards the implementation of passivating contacts in industrial environments are discussed.

In 2017 approximately 1.7% of global electricity demand — representing only 0.28% of total global primary energy consumption — was met by electricity generated by photovoltaic (PV) modules, the vast majority of which comprise crystalline silicon (c-Si) solar cells[1]. These modest statistics belie a transformational change that is occurring in electricity generation worldwide: 2016 saw PV become, for the first time, the fastest growing source of net electricity generation capacity with 74 GW installed; an additional 100 GW of PV was installed in 2017, roughly one-third of all new capacity[1,2]. While crystalline silicon, with a current share of 95% of the PV market[2], is forecast to remain the dominant PV technology for the coming decades, over 70% of c-Si PV production capacity is vested in the fabrication of a low-performance cell design in which the entire rear silicon surface is alloyed with aluminium to form the positive terminal of the device[3]. This cell structure, called the aluminium back surface field (Al-BSF) cell, has a practical upper limit on its power conversion efficiency (PCE) of only ~20%, compared to the theoretical maximum PCE of 29.4%[3,4]. An additional 20% of the current market, employing the more complex passivated emitter and rear cell (PERC) design, is similarly limited to PCEs of around 23–24% (Box 1)[3,5]. Since it is widely recognized that the ongoing success of the c-Si PV industry is predicated on the sustained increase in cell and module efficiency coupled with a continuing decline in production costs[6,7], simple, innovative solar cell designs that exceed these empirical limits are vital for the continued advancement of c-Si PV.

The most salient common feature that limits the PCE of the Al-BSF and PERC cells is the direct application of the contacting metal onto the light-absorbing silicon wafer. This intimate metal–silicon contact leads to recombination losses of the photogenerated electrons and holes due to a high density of electronically active states at the silicon–metal interface that lie within the silicon bandgap. The use of high temperature functional-impurity doping beneath the metal terminals (the phosphorus and aluminium dopants at the electron and hole contacts, respectively, of the Al-BSF and PERC cells) partially alleviates this effect, reducing the defect-assisted Shockley–Read–Hall contact recombination rate and dramatically lowering the contact resistance. However, absorber doping induces its own fundamental optoelectronic energy losses—notably Auger recombination, bandgap narrowing and free carrier absorption—which limit the device performance[8–11].

To mitigate these deleterious effects, so-called passivating contacts are being developed, which can further reduce contact recombination losses via the insertion of passivating thin films (commonly silicon oxide, SiO_x; or hydrogenated amorphous silicon, a-Si:H) between the silicon wafer and the overlying metal terminals. Some passivating contact technologies remove the dopants from the absorber material altogether, incorporating them into a contact structure that is external to the c-Si wafer. An archetypal example of such a device structure is the silicon heterojunction (SHJ) cell (Box 2). In addition, dopant-free passivating contact approaches are also being explored which, in principle, offer a means of effectively eliminating the aforementioned energy loss mechanisms that constrain the efficiency in c-Si solar cells with heavily doped contacts.

Following the passivating contact approach a spate of record efficiencies, the first to match or surpass the long-held 25% record set by a high efficiency PERC cell design[12,13], were achieved in 2014/15 on devices fabricated on large-area wafers: by SunPower (25%; now 25.2%)[14,15], Kaneka (25.1%)[16] and Panasonic (25.6%)[17]. On the laboratory scale, research at the Fraunhofer Institute for Solar Energy Systems in 2015 yielded a small-area device (4 cm^2) featuring a full-area rear-side passivating contact with a PCE of 25.1%[18], now 25.7%, a record for a device with both sides contacted[19]. Kaneka, after moving to an interdigitated back contact (IBC) cell architecture to maximize light coupling into the c-Si absorber, reported a device with a certified efficiency of 26.7%—the current high watermark for c-Si solar cells[20,21].

Put into historical context, in the past four years c-Si PV research has yielded an additional 1.7% absolute improvement in record device efficiency, compared to just 1.8% over the preceding 25 years[12]. This progress is highlighted in Fig. 1a, which plots the recent rise in passivating contact cell efficiencies, as well as the historical

---

[1] King Abdullah University of Science and Technology (KAUST), KAUST Solar Center (KSC), Thuwal, Saudi Arabia. [2] Department of Electrical and Electronic Engineering, University of Melbourne, Melbourne, Victoria, Australia. [3] Department of Electrical Engineering and Computer Sciences, University of California, Berkeley, California, USA. [4] These authors contributed equally to this work: Thomas G. Allen, James Bullock. *e-mail: stefaan.dewolf@kaust.edu.sa

Box 1 | Fabrication of Al-BSF and PERC cells

The vast majority of commercially manufactured c-Si solar cells, commonly called Al-BSF solar cells, are processed with only five main fabrication steps (texturing; front phosphorus diffusion; silicon nitride, SiN_x, deposition; screen printing and co-firing of the metal electrodes). This simplicity is a result of the fact that many of the processes and materials combine to enact multiple functions in the device. For example, the phosphorus diffusion getters bulk impurities, establishes a low contact resistance at the silicon/metal interface, mitigates the effects of surface defects on recombination and enables lateral charge transport between the front metal fingers. The SiN_x layer further passivates surface defects at the non-contacted, phosphorus diffused, textured front side of the device; it also acts as an anti-reflection coating (ARC) and passivates bulk defects after contact firing via hydrogenation. The aluminium screen-printed paste, sintered at the same time as the front screen-printed silver grid, alloys with the silicon surface, undergoing a melt–recrystallization process leaving a heavily doped p^+ region under the remaining Al metal contact; the etching of the SiN_x by glass frit in the Ag paste ensures the formation of the metal contact to the n^+ silicon surface.

This simplicity in manufacturing has enabled low cost, high throughput production at the expense of device performance. Recombination at the rear contact constrains the PCE to ~20%, so Al-BSF cells are typically fabricated on lower quality multicrystalline wafers. PERC devices are manufactured in a similar way to the Al-BSF cell but with rear-surface passivation (often aluminium oxide, AlO_x) and localized aluminium BSF contacts (typically defined by laser ablation of the AlO_x layer). The addition of the passivation layer at the rear suppresses surface recombination, thereby increasing the device voltage relative to the full-area Al-BSF cell. For this reason, PERC cells have a higher efficiency potential and benefit from being fabricated on monocrystalline silicon wafers with higher bulk lifetimes.

An additional upgrade to the PERC design comes in the form of the so-called selective emitter. Here, a very heavy diffusion aligned directly underneath the front metal grid enables the formation of a low contact resistance and minimizes contact recombination. Outside of the contact region, where the surface defects are passivated with SiN_x, a lighter diffusion, with reduced Auger recombination and parasitic free carrier absorption, is utilized, optimized for lateral charge transport (in concert with the front metal grid pattern). With additional technological advancements—for example, using Al paste with boron additives to increase the dopant density in the local BSF; and continued improvements in p-type silicon bulk lifetime, front metallization, and surface passivation—the PCE of PERC cells in manufacturing environments are expected to reach 24%[5]. However, all of the additional processing steps add complexity, and therefore cost, to the manufacturing process, impacting the potential viability of high-efficiency PERC concepts relative to simpler high-efficiency cell designs with passivating contacts.

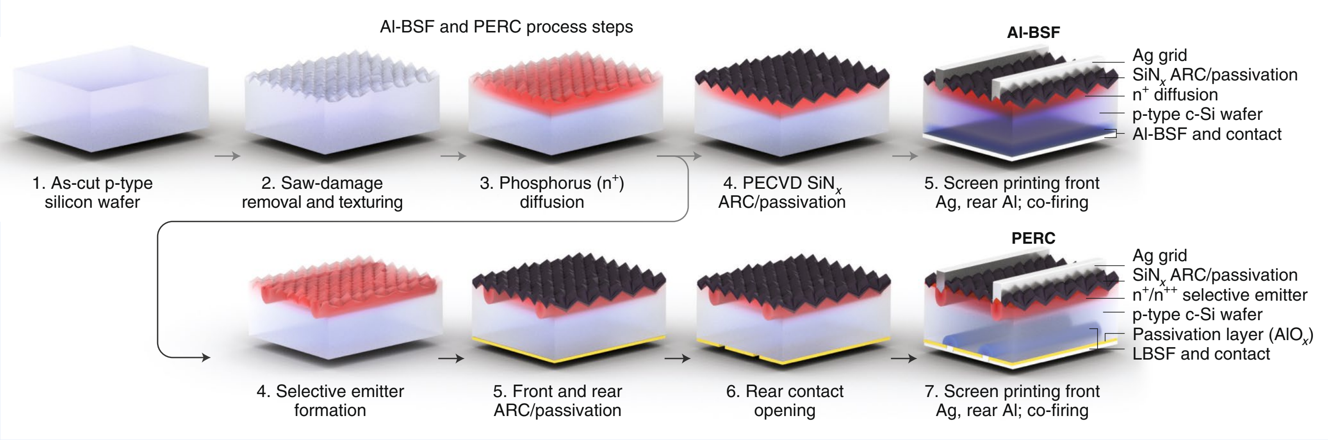

development of technologies with heavily doped, directly metallized contacts. Tellingly, all of the devices with efficiencies greater than 25% feature passivating contacts. Indeed, the most successful devices have both their electron and hole contacts passivated. And while it is remarkable that these high-performance devices have come from a variety of cell architectures (full-area, front- and rear-side contacted[16,18,19]; partial-area, all-back contacted[14,15,17,20,21]), the common path to achieve high performance solar cells is clear: passivating the contact regions of the device.

This article reviews the various conceptual designs and material combinations used to fabricate passivating contacts on c-Si, as well as solar cell architectures that incorporate passivating contacts. In doing so we elucidate the physics of contact formation and the historical progression that has led to this surge in efficiency gains, and critically evaluate the manufacturing potential of these emerging technologies. As such, this review provides an overview of concepts and materials related to contact formation and passivating contacts. For detailed examinations of surface passivation[22–25], contact formation[26,27], fabrication techniques and additional material details in the specific context of passivating contact formation[24,28,29], we direct the reader to other review articles in the literature.

Carrier selectivity and Fermi level pinning

In order for a solar cell to function there must be an internal physical mechanism that spatially separates photoexcited electrons and holes within the light-absorbing semiconductor, resulting in their extraction at the negative and positive device terminals, respectively[30]. This process of charge-carrier selectivity at the terminals implies an asymmetric internal flow of charge carriers towards the solar cell's contact regions: that is, a strong electron and weak hole current towards the electron contact, and vice versa for hole and electron currents towards the hole contact[31].

On the device level, the suppression of the current of non-collected charge carriers to the contact of opposite polarity (for example, holes to the electron contact) is strongly reflected in the open circuit voltage (V_{oc}) since these non-collected carriers recombine at the contact, reducing the electrochemical potential of the system and so lowering the device voltage. The energy losses associated

Box 2 | Monofacial, bifacial and IBC silicon heterojunction devices

A relatively simple passivating contact device design is that of the silicon heterojunction cell (SHJ), which takes the doping outside of the c-Si absorber and places it within the contact structure in the form of n- and p-doped a-Si:H layers. The SHJ device architecture, like the Al-BSF cell, benefits from a conceptually facile fabrication procedure: a thin film of intrinsic a-Si:H is sandwiched between the silicon wafer and the doped a-Si:H layers in order to passivate surface defects, resulting in high operating voltages; a transparent conductive oxide (TCO; typically sputtered indium tin oxide, ITO) provides lateral charge transport to the screen printed metal fingers and acts as the ARC.

The most critical performance limitation of this design is parasitic absorption in the front TCO and a-Si:H layers, spurring research into alternative materials and device designs. One solution to this problem is to place all of the contacts on the rear side of the wafer in an IBC architecture. Alongside the increase in fabrication complexity, the transferral of the front contacts to the rear side of the cell places stricter requirements on both the electron and hole contact resistivities owing to their relative reduction in surface area. In addition, since the vast majority of excess carriers are photo-generated at the front of the wafer, high bulk lifetimes and state-of-the-art surface passivation is necessary to achieve the long diffusion lengths needed to maintain a high quantum efficiency.

A simpler strategy to improve the energy yield of conventional SHJ cells is to move toward bifacial designs. Bifacial cells can absorb light from both the front and the rear side of the device, thereby collecting the otherwise rejected environmental albedo radiation, resulting in a relative increase in sunlight absorbed within the cell, and so potentially higher energy output. Since the bifacial device absorbs albedo radiation from the rear side of the cell, the increases in energy yield from bifacial cells and modules are heavily dependent on location and environmental factors, as well as cell and module design. However, to further improve the short wavelength response, both the mono- and bifacial configurations, highly transparent contact materials, TCOs, and passivating interlayers are needed. Wide-bandgap, dopant-free materials are particularly promising transparent alternatives to the doped a-Si:H electron and hole transport layers (ETLs and HTLs), already showing increased currents on the device level.

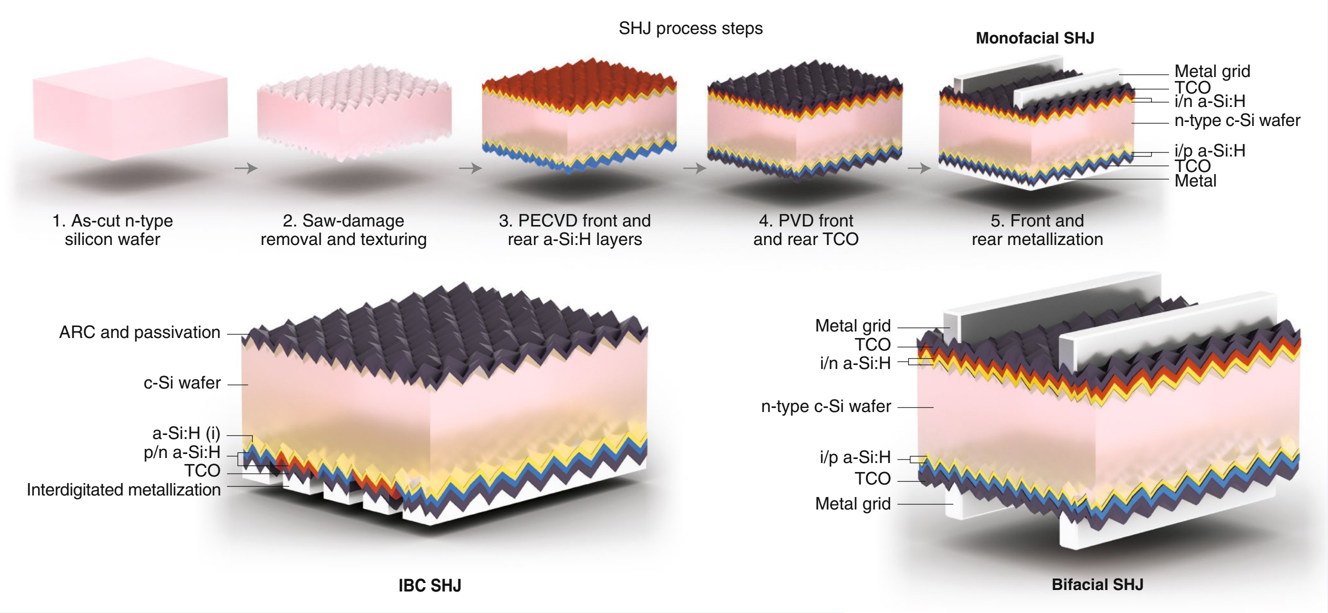

with the collected current (electrons passing through the electron contact) manifest in the series resistance of the device which strongly influences the fill factor (*FF*). Figure 1b, which plots the *FF* versus V_{oc} for those cell configurations in Fig. 1a for which the data are available, shows that passivating contacts have enabled more advantageous FF/V_{oc} combinations compared to cells with heavily doped contacts, indicative of enhanced charge-carrier selectivity[32].

At a fundamental level, the asymmetric internal currents that are a consequence of charge carrier selection are governed by both the conductivity, σ_e and σ_h, and the gradient in electrochemical potential, grad(η_e) and grad(η_h), for electrons and holes throughout the bulk material leading toward the contact areas[30,33], as shown in the conceptual solar cell diagram in Fig. 2. Unfortunately, these parameters are difficult to extract experimentally and instead, in c-Si devices, a pair of equilibrium parameters are typically used to provide a simple, first-order approximation to model the solar cell operation under illumination: the saturation current contribution from contact recombination J_{0c} to represent the flux of non-collected charge carriers to the contact, and the contact resistivity ρ_c to represent the interface resistance presented to collected charge carriers. It follows that an effective, highly selective contact is one that minimizes both recombination (J_{0c}) and resistive losses (ρ_c). It is important to be aware that this model of solar cell operation is not applicable to, for example, so-called non-ideal recombination where the value of J_{0c} varies with illumination, and non-Ohmic contacts, in which the value of ρ_c cannot reliably be defined, and is, by definition, non-linear with applied voltage. In such cases, more detailed device modelling is required[34].

A secondary parameter to be considered is the fraction of the solar cell's surface area that is contacted, f_c. In the case of a partial contact fraction ($f_c < 100\%$), a state-of-the-art surface passivation layer (for example, AlO_x or SiN_x) can cover the non-contacted area,

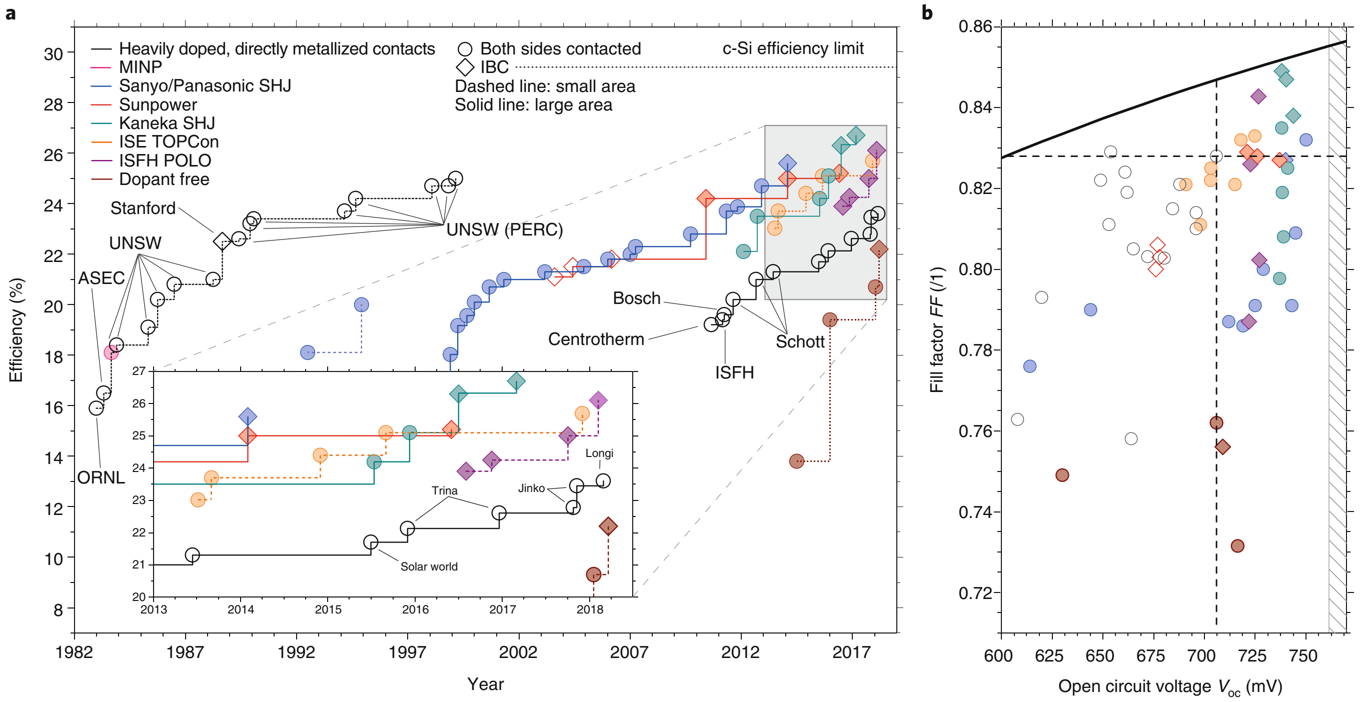

Fig. 1 | Historical progression of notable c-Si solar cell efficiencies. **a**, The solid, coloured data points represent passivating contact devices; open data points represent heavily doped, directly metallized contacts; circles indicate both sides contacted designs; and diamonds represent IBC designs[12,15–21,35,69,71,81,126,127,129,147–176]. The red open diamonds represent Sunpower devices fabricated prior to their explicitly mentioning the use of passivating contacts in the device structure. Record efficiencies of large-area industrial PERC cells (open circles, solid line) are approaching the efficiency ceiling of this device design, foreshadowing a shift in production towards passivating contact cell architectures. The theoretical efficiency limit for c-Si solar cells (29.4%) is represented by the dotted line. Inset: details of recent results, highlighting the progress in passivating contact cell structures. **b**, *FF* vs. V_{oc} for the cell types in **a** for which data is available[15–19,21,35,69,71,81,126,127,129,147–156,159,160,162,163,168–172,174–183]. For reference the V_{oc} for the optimum c-Si cell efficiency is represented in the vertical hatched line[4], and the empirical relationship describing the influence of V_{oc} on *FF* of Green[184] is plotted. The FF/V_{oc} data of the 25% PERC cell (the highest efficiency obtained to date utilizing the heavy doping approach) is represented by dashed lines. All data are tabulated in Supplementary Data 1.

reducing the global J_0 and increasing the device voltage. Indeed, it is the partial rear-contact fraction and rear-surface passivation that differentiates the Al-BSF from the PERC cell structure. This improvement in global J_0 must be balanced against an increase in both the cell's series resistance, due to the smaller contact area, and fabrication complexity.

A conceptually simple method to achieve carrier selectivity is to apply conductive layers (for example, metals) directly to the silicon wafer with asymmetrical work functions (ϕ) relative to the c-Si conduction and valence band edges. In this way, following Schottky–Mott theory, the work function of the outer metal can be used to manipulate the surface potential of the underlying silicon wafer, with electrons (holes) accumulating at the low (high) work function interface, displacing minority carriers and reducing the J_{0c}[34–36]. With the proper choice of contact metal, the energetic barriers that impede the transfer of charge at the contact interface (that is, the Schottky barrier, ϕ_B) can be made sufficiently small to enable the formation of a low-resistance contact by thermionic emission at room temperature (Fig. 3b).

In practice, the formation of carrier-selective contacts via direct metallization is complicated by the existence of surface phenomena such as dangling bonds, metal induced gap states (MIGS) and interface dipoles, which are not accounted for in Schottky–Mott theory[26]. As a consequence, the metal work function is unable to manipulate the concentration of carriers at the semiconductor surface to a significant extent. This commonly results in the formation of a significant Schottky barrier at the semiconductor surface regardless of the metal work function—behaviour which has been termed Fermi level pinning (FLP). The influence of FLP on the silicon surface, empirically demonstrated in plots of barrier height versus metal work function[26,27], indicate a strong pinning effect that typically results in the depletion of charge carriers from the contacted silicon sub-surface, as shown in Fig. 3c, for most metal–silicon contacts.

To work within the constraints imposed by FLP on directly metallized surfaces, either the work function of the contact material has to take extreme values to lower the barrier height, Φ_B[37,38], or the width of the depletion region within the semiconductor, W, has to be narrowed (for example, via heavy doping) so that quantum mechanical tunnelling of charge carriers through the Schottky barrier can occur, as shown in Fig. 3d. The efficacy of the heavy doping approach is shown in Fig. 3f which plots experimental ρ_c values versus surface doping concentration for p- and n-type surface doping (N_A and N_D). However, heavy doping results in an Auger-limited floor in the recombination at directly metallized contacts of $J_{0c}>\sim 200$ fA cm^{-2}, two-to-three orders of magnitude greater than state-of-the-art passivated, non-metallized surfaces[9,10,39]. This is shown empirically in Fig. 3g which plots J_{0c} as a function of sheet resistance of an unpassivated heavily doped region (used here as a proxy for overall doping level in the diffused silicon sub-surface). With increased doping, and so decreasing sheet resistance, the J_{0c} plateaus as the Auger recombination contribution (dashed lines in Fig. 3g) dominates the measured value, thereby constraining the selectivity of heavily doped, directly metallized contacts. An alternative (or complementary) route to contact formation is to apply a passivating interlayer between the semiconductor and contact material to 'de-pin' the Fermi level—the passivating contact approach (Fig. 3e).

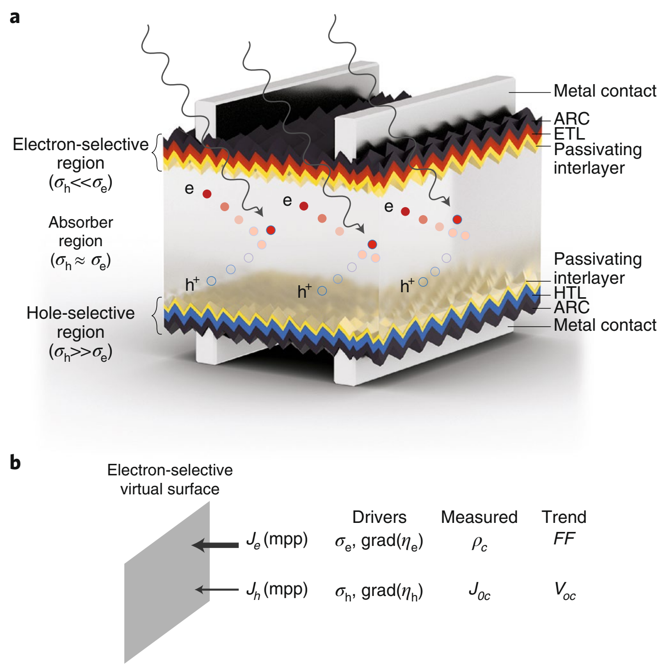

Fig. 2 | Conceptual schematic of the operation of a solar cell. a, Absorbed photons (wavy arrows) generate free electrons and holes (represented in this and all other Figs. by red and blue colours, respectively) that are directed toward their respective contacts via the formation of charge carrier selective regions. The features of a typical passivating contact cell design are identified on the right-hand side of the cell schematic. **b**, The electron-selective virtual surface summarizing the physical mechanisms that drive carrier selectivity (σ; grad(η)), the empirically probed values (ρ_c; J_{0c}), and their general influence at the cell level (*FF*; V_{oc}). A good charge carrier selective region will maximize the flow of the selected carrier (electrons in the electron-selective virtual surface above, represented by the thick arrow) at maximum power point (mpp), $J_{e(mpp)}$, and minimize the flow of the non-selected carrier, that is, holes or $J_{h(mpp)}$ (represented by the thin arrow), via the suppression of recombination.

Passivating contacts: materials and devices

Due to the inherent limitations of directly metallized, heavily doped contacts, considerable effort has been devoted towards the alternative concept of passivating contacts. Rather than invoking the compromises implicit to heavy doping, passivating contacts directly address recombination losses and FLP effects at the c-Si surface, most commonly by integrating a thin passivating interlayer between the c-Si surface and the outer electrode. The passivating interlayer not only passivates the c-Si surface but also physically separates the c-Si absorber from overlying metallic layers, which would otherwise induce energy states within the silicon bandgap (via MIGS)[40]. Additionally, the suppression of FLP introduces a range of potential mechanisms that can be used to achieve carrier selectivity. These include the exploitation of asymmetries in band offsets, work functions, tunnelling probabilities and charge-carrier mobilities at the c-Si/contact interface, as well as the use of energy-selective defect bands[30,33,41,42]. Thus far, the most successful and empirically realizable of these strategies involves the use of heterocontacts with asymmetric work functions on top of a thin passivating layer applied to the c-Si surface.

Passivating contacts also have several practical advantages over conventional contacting schemes. Compared to directly metallized, heavily doped contacts, passivating contacts are typically characterized by a very low J_{0c}. Hence they can be applied in simple large-area (f_c up to 100%) configurations, in contrast to heavily doped contacts[43]. The ability to apply passivating contacts in a large-area configuration not only simplifies device fabrication but also means that a higher ρ_c can be tolerated: values as high as ~100 mΩcm^2 can result in no significant PCE loss for full-area contacts (see below)[27,43]. When applied to the rear of a cell in a so-called hybrid architecture (Fig. 4b), such passivating contact configurations also simplify the current flows in the device to one dimension, eliminating lateral resistive losses[18] and permitting the use of lower doping concentrations in the c-Si absorber. Finally, the high temperatures (≥750 °C) required to make heavily doped contacts, and the associated necessity for cleanliness throughout the fabrication process, are relaxed when dealing with many passivating contact technologies, some of which can be deposited at or below 100 °C[44,45]. However, lower fabrication temperatures, and the disabling of impurity gettering (for example, by removing the phosphorus diffusion step) in some passivating contact cell structures, require high purity wafers with stable bulk lifetimes in their pre-processed state. In addition, cells with passivating contacts on both sides of the device require a lateral charge transport mechanism, typically a TCO, as an alternative to a front-side diffused surface, which can adversely affect the J_{sc}.

Metal–insulator–semiconductor passivating contacts. Early attempts at contact passivation on c-Si solar cells took the form of metal–insulator–semiconductor (MIS) contacts. During the 1970s and 1980s a range of different structures were proposed for passivating contacts featuring different metals and passivating insulator layers[36,46–49]. A particularly striking example is that of the metal–insulator–semiconductor–insulator–metal (MISIM) cell proposed by Green[36] and later realized by Tarr et al[47]. This cell design mimics the simple contacting arrangement described above—using two metals with asymmetric work functions as electron and hole contacts—with a thin silicon oxide interlayer to physically separate the metal from the silicon wafer and passivate surface defects. However, a lack of affordable, high-work-function metals limited the applicability of the MISIM cell structure. Instead, the MIS inversion layer (MIS-IL) cell structure received comparatively more attention. The archetype of the MIS-IL family, a p-type cell with a front electron MIS contact, and a rear Al-BSF hole contact, is shown in Fig. 4a. The front electron contact features a combination of thermally evaporated Al and a tunnelable (~15 Å) thermally grown SiO$_2$ layer[50]. The benefits of the MIS approach were demonstrated through improvements in V_{oc}, as highlighted by Godfrey and Green in 1979, who reported a V_{oc} of 655 mV, 20 mV higher than any previously reported c-Si device[49]. These MIS cells relied on a silicon monoxide ARC, deposited in the non-contacted areas, with a positive fixed-charge density to form an electron inversion layer at the surface. In this way, the fixed-charge density in the non-contacted areas performs a similar role to that of the metal work function in the contacted areas. The effect of the fixed charge density was later enhanced through the application of PECVD SiN$_x$, and later Cs$^+$ ion incorporation, to increase the magnitude of positive charge, aiding in the formation of the induced inversion layer[51–53].

After reaching a peak PCE of 19.6% in 2001[54], further development of the MIS-IL architecture stalled as other contact approaches garnered more research attention. One such example is the 'metal–insulator–NP' (MINP) cell concept. MINP cells utilized a hybrid front contact, with an MIS contact formed on top of a lightly dopant-diffused surface, with the intention of providing benefits in terms of lateral resistance and recombination[55]. Using a Ti/SiO$_x$/c-Si(n$^+$) front MIS electron contact, this cell structure held the c-Si efficiency record for a short time in the 1980s becoming the first silicon device with a PCE over 18% (Fig. 1a)[56]. Since then, the use of MIS contacts on lightly diffused surfaces has been explored with different metals and insulators being featured in both n- and p-type cells with efficiencies above 21%[57–59].

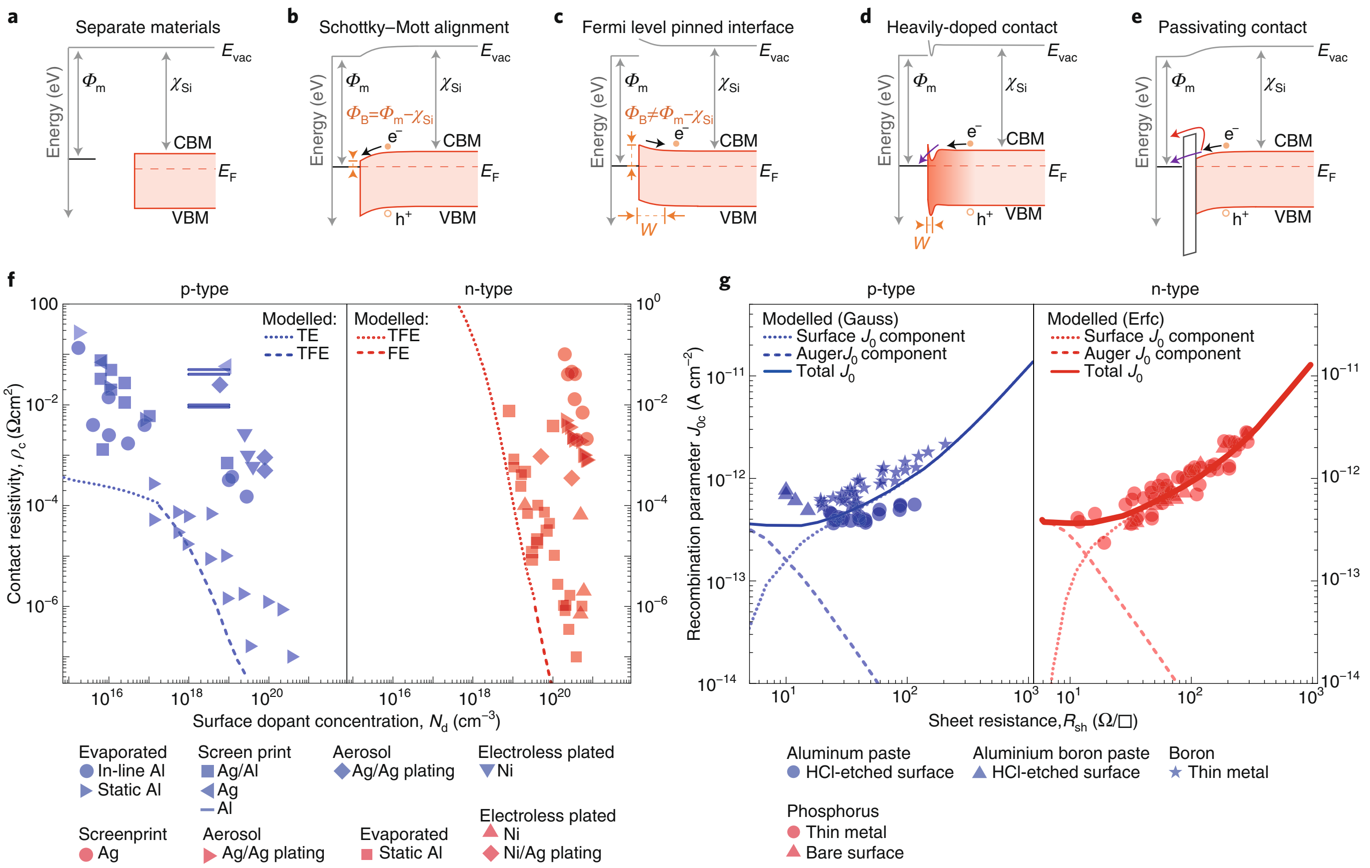

Fig. 3 | Motivation for, and characteristics of, heavily doped contacts. **a**–**e**, The Schottky–Mott relationship implies facile manipulation of the semiconductor surface potential (**a**, **b**) via the application of metals (black line in **b**–**e**) of appropriate work function (Φ_m) relative to the semiconductor's electron affinity (χ). In practice, Fermi level pinning dampens this effect, often resulting in the depletion of charge carriers from the surface (**c**). To improve the selectivity of these contacts, either the width (W) of the barrier (Φ_B) has to be narrowed to allow for the tunnelling process to occur (purple arrow), as in the heavy doping approach (**d**), or the Fermi level has to be 'de-pinned' (by applying a passivating interlayer, represented in white in **e**), such that the semiconductor's surface potential can be influenced by the overlying contact material, facilitating tunnelling or thermionic emission (red arrow) through the contact structure: the passivating contact approach (**e**). **f**,**g**, The efficacy of heavy doping, in terms of ρ_c[27,185–202] (**f**) and J_{0c}[9,10,203–206] (**g**). The ρ_c trend was modelled using thermionic emission, thermionic-field emission or field emission models (whichever is dominant at the specific dopant concentration)[207], with the barrier heights (Φ_B) and tunnelling effective masses (m_e) of $\Phi_B = 0.35$ eV and $m_e = 0.4m_0$ on p-type surfaces, and $\Phi_B = 0.6$ eV and $m_e = 0.3m_0$ on n-type surfaces. Contacts featuring Al doping are represented as a line, centred around the solid solubility limit of Al in Si at typical peak firing temperatures, to convey the uncertainty in surface doping concentration[203]. The J_{0c} trend was modelled in EDNA2[208,209], assuming an infinite surface recombination velocity and error (Erfc) and Gaussian (Gauss) functions for the phosphorus and boron diffusion profiles, respectively. The Auger and surface recombination components of the total J_0 are represented by the dashed and dotted lines in **g**, respectively. For the empirical data in **g**, all values of J_{0c} have been corrected to the same value of the intrinsic carrier density in silicon, $n_i = 8.59 \times 10^9$ cm^{-3}, wherever possible. All data are tabulated in Supplementary Data 1; some data sets are a compilation from multiple sources. We note that some of the ρ_c results were obtained from samples in which a metal layer is fired through a dielectric layer(s).

The external doping approach. A parallel stream of research initiated in the 1980s involved the development of passivating contacts with polycrystalline silicon (poly-Si)[60,61] and semi-insulating polycrystalline silicon (SIPOS) based material systems[41,62]. These inherited strongly from earlier research into microelectronic devices[63], and were typically composed of a thin SiO$_x$ layer sandwiched between the heavily-doped silicon-based outer layer and the c-Si wafer. By the mid-1980s doped poly-Si and SIPOS contacts with thin chemically and thermally grown interfacial SiO$_x$ layers were found to provide low J_{0c} and ρ_c on c-Si[62,64], to the extent that SIPOS based contacts were the first to demonstrate a V_{oc} above 700 mV—a significant milestone at the time[41].

The physical mechanism that determines the performance of poly-Si based contacts is complicated by in-diffusion of dopant atoms from the poly-Si into the c-Si wafer, which is almost universally reported for such contacts. This renders poly-Si contacts conceptually akin to the MINP, rather than MIS, design, although the dopant dose entering the c-Si absorber is typically low and hence does not significantly incur the deleterious heavy doping effects associated with the Al-BSF and PERC cells. The small amount of in-diffusion occurs during the high temperature steps (>700 °C) required for both SIPOS and poly-Si based contacts, in some cases assisted by the formation of pinholes in the thin SiO$_x$ layer[65]. As such, the oxide thickness, preparation method and thermal budget all play critical roles in determining the contact properties[66,67]. Hydrogenation treatments of the SiO$_x$/Si interface, for example, by capping the annealed poly-Si with hydrogen-rich SiN$_x$ or AlO$_x$, exposure to hydrogen plasma, or via the release of hydrogen from the doped silicon film itself during the high temperature anneal, have been demonstrated to have a beneficial effect on the J_{0c}, indicative of the substantive role of the defect passivation provided by the SiO$_x$ interlayer in the poly-Si contact structure[68]. A thorough

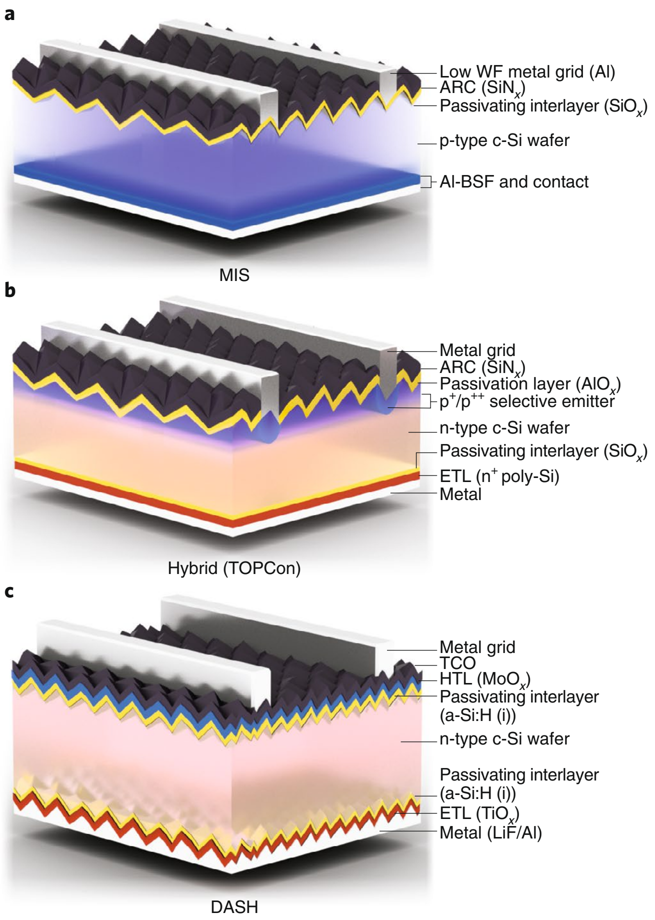

Fig. 4 | Solar cells featuring passivating contacts. a, The hybrid MIS cell, featuring a front electron MIS contact and a rear Al-BSF hole contact, is one of the original demonstrations of passivating contacts on c-Si solar cells. **b**, The TOPCon solar cell is another hybrid cell, featuring a front side boron diffused selective emitter for the hole contact and a rear phosphorus doped poly-Si electron contact. **c**, The DASH solar cell utilizes a set of dopant-free metal oxide and fluoride electron and hole transport layers to replace doped silicon layers.

review of poly-Si passivating contacts, including deposition methods and hydrogenation treatments can be found in the review of Schmidt et al[24].

Recent years have seen a revival in interest in poly-Si contacts for c-Si solar cells. The current state-of-the-art polysilicon contacts can be implemented via a range of different deposition and doping techniques, exhibiting J_{0c}< 5 fAcm^2 and ρ_c< 2 mΩcm^2 for both n-type and p-type contacts[24,69,70]. At the device level, a particularly promising hybrid structure, being developed by several groups, is shown in Fig. 4b which features a full-area n$^+$ poly-Si rear contact and a boron diffused front hole contact[19]. This hybrid structure, sometimes referred to as the tunnel-oxide passivating contact (TOPCon) solar cell, was recently demonstrated at 25.7%[19]. Following shortly after this, an all poly-Si contacted IBC device was also demonstrated with a PCE of 26.1%, the highest efficiency achieved for a solar cell with both n$^+$ and p$^+$ poly-Si contacts[71].

The early 1990s saw the development of a low temperature (≤200 °C) alternative passivating heterocontact utilizing a stack of intrinsic and doped hydrogenated a-Si:H layers, now known as the silicon heterojunction (SHJ) contact (Box 2). This structure was inherited from earlier research on a-Si:H/poly-Si tandem cells[72], and the known surface passivation of c-Si by thin films of a-Si:H[73]. Work on SHJ cells was pioneered by Sanyo (later acquired by Panasonic) and trademarked as the 'Heterojunction with intrinsic thin-layer' or HIT cell[74]. Optimization of the SHJ structure over the following decade resulted in an efficiency increase from 14.5% to above 20% by the year 2000 (ref. [75]), marking its competitiveness with conventional dopant-diffused homojunction technologies.

Conceptually and practically, SHJ contacts, compared to the poly-Si/SiO$_x$ structure described above, more closely resemble the MIS passivating contact archetype: a passivating interlayer (intrinsic a-Si:H) alleviates FLP, allowing the outer layer (boron or phosphorus doped a-Si:H) to manipulate the c-Si surface potential—providing a selective conductive pathway for the collected carrier. Physically, the major difference between the SHJ and poly-Si contacts is in the charge transport at the contact interface. For SHJ contacts, direct tunnelling from the silicon wafer into the doped a-Si:H layer is not a likely transport mechanism owing to the relative thickness of the intrinsic a-Si:H passivation layer (~5 nm), and so bulk current transport through the contact structure and thermal transport over energy barriers at the contact interfaces dominate ρ_c (refs. [76,77]). In addition, unlike in the poly-Si contacts where a dopant tail is often present underneath the c-Si surface, the dopants in the SHJ contact structure are strictly confined to the outer a-Si:H layers, placing stringent requirements on the surface passivation provided by the intrinsic a-Si:H. The induced surface potential in the c-Si wafer therefore plays a more prominent role in the SHJ structure. Consequently, the low doping efficiency of boron in a-Si:H can lead to inadequate band bending at the c-Si surface, and so *FF* issues attributed to injection-dependent recombination at the hole contact[78,79].

The most commonly ascribed shortcoming of the SHJ approach in terms of its ultimate performance is the parasitic absorption occurring in the front a-Si:H layers and TCO (typically ITO) that provides lateral charge transport[80]. Recent PCE improvements have consequently come from implementing the more complex IBC design, which places both contacts on the rear side of the cell, removing both the TCO and doped a-Si:H from the sun-facing side of the device[17,20]. Other strategies to reduce parasitic absorption without adopting the complex IBC design have focussed on thinning the a-Si:H films[81], diluting them with carbon and oxygen[82–84], replacing the doped a-Si:H with nano-crystalline silicon and silicon oxide[76,85,86], and investigating alternatives to ITO[87]. Indeed, numerical device modelling indicates that widening the bandgap of the deposited layers in the SHJ contact configuration can also have beneficial impacts on V_{oc} and *FF*[79]. Regardless, the SHJ approach remains the most successful c-Si cell architecture in terms of efficiency—first claiming the world record in 2014 (ref. [17]) and continuing to maintain this lead over the past 5 years[20,21].

Towards dopant-free passivating contacts. A final passivating contact approach is the integration of dopant-free materials into the contact structure to replace the doped silicon layers or regions described above. The term 'dopant-free' used here refers to the avoidance of doped-silicon, an acknowledgment of the fact that many dopant-free materials are doped with native defects (or even extrinsically). These dopant-free materials include metal compounds (most notably metal oxides), low-dimensional semiconductors and organic materials. Driving the rapid growth of this research area, largely an extension of the work on MIS contacts, is the potential to overcome the performance limitations of existing passivating contacts. As reflected in the electronic band alignment diagram in Fig. 5, the use of silicon-based passivating contact films as electron and hole transport layers permits only a limited range of band gaps and work functions—which in turn limits the optical and electrical design of the contact. In contrast, materials such as

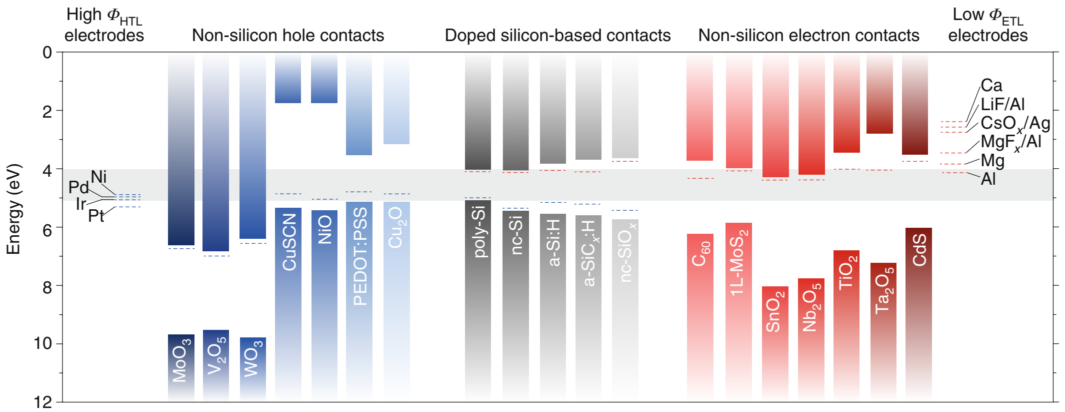

Fig. 5 | Materials for passivating contacts. Conduction and valence band positions (upper and lower rectangles, respectively), and indicative Fermi level positions (dashed lines) of various metals, metal compounds and organic semiconductors, with ETLs in red and HTLs in blue[27,90,104,127,210–227]. The band edges of c-Si are shown as a grey bar for reference. It should be noted that these energy levels are based on measurements of pristine thin films, the magnitude of which are not always achieved in electronic devices (particularly the high-work-function n-type oxides). In addition, many of these materials are subject to a significant spread in valence band, conduction band and Fermi level positions (an effort has been made to choose values in the middle of reported ranges) — this is particularly true for the silicon-based films, the characteristics of which are heavily dependent on their stoichiometry and doping concentration. All data are tabulated in Supplementary Data 1.

metal oxides introduce a more diverse materials space with a wider range of work functions outside of the confines of the c-Si band edges, as well as potentially more suitable optical characteristics for the front and rear sides of the device (such as wider bandgaps for increased transparency of high energy photons, reduced parasitic free-carrier absorption at the front and rear of the device, and a broader range of refractive indices for optimal front ARC and rear reflector formation). In addition, such materials can generally be deposited using simple, low-temperature, physical vapour deposition or even solution-based processing techniques—introducing potential reductions in fabrication costs over doped poly-Si or a-Si:H passivating contacts.

The most widely studied dopant-free contact material subgroup are those based on metal oxides. At the electron contact, a number of n-type metal oxides with favourable theoretical band alignments, and in some cases silicon surface passivation, are being explored, for example, TiO_x (refs. [88,89]), NbO_x (ref. [90]), TaO_x (ref. [91]), GaO_x (ref. [92]), ZnO_x (ref. [93]), CsO_x (ref. [94]), some of which were previously identified during early semiconductor–insulator–semiconductor research beginning in the 1970s[95,96]. The most prominent of the above metal oxide electron transport layers (ETLs) is TiO_x, already being successfully integrated into hybrid cells (that is, with a front dopant diffusion), as full-area[97] and partial-area rear contacts (PRC)[89] with an efficiency in excess of 23% recently demonstrated[98]. Equivalent hole contact materials, p-type metal oxides with favourable valence band alignment with c-Si, are less abundant than the n-type metal oxide ETLs, though some attention has been paid to CuO_x (ref. [99]). In fact, most research in recent years has focused on the n-type transition metal oxides, including MoO_x (refs. [35,100–102]), WO_x (ref. [102]), and VO_x (ref. [103]), which, as shown in Fig. 5, feature very high work functions (above 6.5 eV in the ideal case)[104]. Molybdenum oxide in particular has recently been integrated into PRC and full-area contact cells attaining PCEs of 20.6%[105] and 23.5% (J. Dréon, C. Ballif & M. Boccard, Influence of MoO_x and (i)a-Si:H layer thickness on the properties and stability of c-Si heterojunction solar cells, presented at the 2019 Spring Meeting of the European Materials Research Society).

In addition to metal oxides, a range of other metal compounds have been explored as contact materials for c-Si solar cells, including sulphides[106], nitrides[107,108], phosphides[109], iodides[110], carbonates[111] and fluorides[35]. Of note among these are the alkali and alkaline earth metal fluorides utilized in electron extraction, including LiF and MgF_2. As shown in Fig. 5, after the evaporation of a metal overlayer, typically Al, these contact structures exhibit very low work function values. This is commonly associated with the formation of a molecular dipole, which offsets the energy band alignment between the c-Si and outer electrode[112]. Owing to this, Al/LiF bilayer contacts, for example, achieve unusually low ρ_c on n-type c-Si and hence have been used directly as a PRC in an n-type cell—an architecture which was not previously possible due to the difficulties of contacting n-type c-Si without dopants[113]. Other related contacting techniques, such as the use of high-*k* dielectric bi-layers to generate interfacial dipoles[114], or the exploration of chalcogenide passivation (S and Se) as alternatives to tunnel oxides[115], remain largely unexplored in c-Si PV and could offer promising approaches to fabricate passivating contacts.

Two less developed dopant-free passivating contact subcategories are those formed by low-dimensional materials and thin films based on organic compounds and polymers. Devices featuring low-dimensional carbon-based contacts, namely graphene[116] and carbon nanotubes[117], as well as the inorganic transition metal dichalcogenides, such as MoS_2 (ref. [118]), have thus far failed to enable PCEs above 15%, with most falling below 10%, owing largely to a lack of surface passivation. The use of small organic molecules or self-assembled monolayers have been comparatively more successful. On silicon, materials like poly (ethylene oxide) (PEO)[119] and 8-hydroxyquinolinolato-lithium (Liq)[120] have been shown to reduce barrier heights and facilitate improvements in electron collection. Recently, monolayers of polar amino acids have also been shown to facilitate electron collection following direct Al metallization on silicon, with an efficiency of 17.5% having been demonstrated utilizing this contacting approach as a full rear contact on an n-type Si wafer[121]. The most exciting results within this category however, have been achieved using polymer based contacts[45,122,123], with PEDOT:PSS proving to be the most successful material. Full rear area PEDOT:PSS contacted cells have attained champion cell efficiencies of 20.6% using industrial cell fabrication processes, comparable to high performance Al-BSF cell efficiencies[124]. The higher V_{oc} potential of the PEDOT:PSS devices over conventional Al-BSF cells further demonstrate the potential of PEDOT:PSS as a hole transport layer (HTL)[125]. However, parasitic absorption in the PEDOT:PSS, limited surface passivation comparable to other passivating contacts,

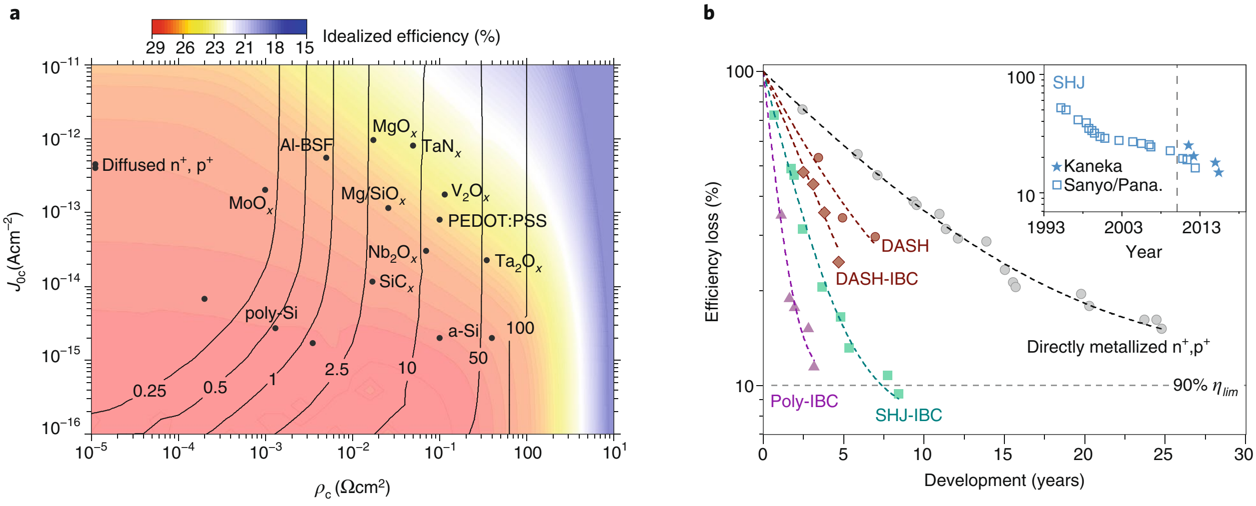

Fig. 6 | Comparison of silicon solar cell contacting approaches. a, Solar cell modelling in which the rear contact parameters (J_{0c} and ρ_c) act as the input and the optimized contact fraction (black lines f_c), and so cell efficiency (coloured contours) is output. The modelling, performed in Quokka 2.0[228], is based on perfect absorption and an idealized front contact. Typical values of directly metallized, heavily doped contacts (Diffused n+, p+; Al-BSF), and different passivating contacts (labelled) are superimposed on the Figure (see Supplementary Data 1 for tabulated data)[24,58,69,90,101,107,122,229–235]. **b**, Comparison of efficiency loss $(1-\eta/\eta_{\rm lim})\times 100$ against development time for heavily doped directly metallized contacts (black) and passivating contact (coloured) technologies (data from Fig. 1a). The data points are fitted using the Goetzberger function (dashed lines)[131], while the dashed horizontal line marks 90% of the fundamental efficiency limit $\eta_{\rm lim}$. Inset: the efficiency loss of both-sides-contacted SHJ technology against calendar year, as reported by Panasonic and Kaneka. The dashed vertical line depicts the expiry of the European patent for this technology.

and questions over long term stability, all remain open issues which have inhibited the further adoption of this cell structure[122].

The rapid improvement in dopant-free contacts is best exemplified by the impressive improvements in cells fabricated using a pair of such contacts. A schematic diagram of this cell architecture, referred to here as the dopant-free asymmetric heterocontact or DASH solar cell, is provided in Fig. 4c. Over the past 4 years, the efficiency of this cell concept has risen from 13.8% to 20.7%[126,127] and from 15.4% to 22.5%[128,129] for both-sides-contacted and IBC cells, respectively, indicating the promise of this approach.

Comparison of contacting approaches

The recent explosive growth of passivating contacting techniques has provided a diverse range of material combinations, highlighted in the above sections, with differing ρ_c and J_{0c} characteristics. While the general goal remains to simultaneously achieve low ρ_c and J_{0c}, this is rarely achieved experimentally for newly developed structures, making it difficult to directly compare the efficacy of dissimilar approaches to contact formation. As discussed above, the contact fraction f_c is a complicating factor as it is an additional lever that can be used to trade-off the relative significance of J_{0c} and ρ_c on the overall cell performance. Fortunately, disparate contacts can still be generally compared via graphical means. Figure 6a shows the simulated ideal solar cell efficiency (coloured contours) resultant from changing the J_{0c} and ρ_c of the rear contact. This plot is generated by calculating the optimum f_c (black lines) for each J_{0c} and ρ_c combination, so that the maximum performance is extracted out of each set of contact characteristics. Experimentalists can superimpose contact data points on such plots to compare the efficacy of different contact structures. Several prominent results are included on this plot which are indicative of the technologies discussed above.

Figure 6a illustrates that contacts with vastly different characteristics can achieve the same level of performance, provided f_c can be altered arbitrarily. As can be seen from their position in Fig. 6a, directly metallized, heavily-doped contacts are characterized by low ρ_c and high J_{0c}, and so a low f_c is optimal. In contrast, many passivating contacts, for example the SHJ contacts, are characterized by a very low J_{0c} and comparatively high ρ_c, and so a high optimal f_c. This re-emphasizes the architectural advantages of the passivating contact technologies. Further, while the directly metallized, heavily doped contacts are fundamentally constrained to their marked positions on this plot, the passivating contacts continue to improve with technological advancements. In terms of ρ_c and J_{0c}, the most promising passivating contacts remain the SHJ and poly-Si technologies, as also reflected in the cell efficiency results discussed above. The dopant-free contacts continue to trail their more developed silicon-based counterparts, but have shown dramatic improvement in recent years. While the efficiency advantages of the passivating contact approaches are becoming more apparent, the remaining challenge in the industrial adoption of passivating contacts is overcoming the inertia behind heavily doped technologies.

Similar conclusions can be drawn from compilations of cell-level experimental results. Figure 6b compares the remaining efficiency loss of cells utilizing heavily-doped directly-metallized contacts (black points) against various passivating contact technologies (coloured points)[130]. The 'initiation' date of each technology is estimated following a similar approach to Altermatt et al.[131], whereby the Goetzberger function is fitted to the historical progression of efficiency records for each technology. While the plot indicates that passivating contact technologies exhibit comparatively faster rates of development (in some cases rivalling the development rate of perovskite solar cells)[131], this is likely attributable to greater investment in resources for research, continuous improvments in silicon wafer quality, metrology and processing equipment, and generally through the accumulated knowledge in the field of c-Si PV available at the time of development. Of course, the true advantage of passivating contact technologies is indeed their higher efficiency potential, as particularly evidenced by the SHJ and polysilicon IBC architectures, already reaching ~90% of the fundamental efficiency limit $\eta_{\rm lim}$ (equivalent to a PCE of ~26.4%)[4]. This is further supported by the practical efficiency limit of each technology, also fitted in the Goetzberger function, which is consistently higher for the passivating contact technologies. Interestingly, the both-sides-contacted SHJ cell technology cannot be well fitted by the Goetzberger function, likely due to its successful patenting which hindered its proliferation throughout its early development, limiting the propagation of accumulated knowledge gained through research into this particular device structure. The inset of Fig. 6b shows the historical progression of both-sides-contacted SHJ cells, initially by Sanyo/Panasonic. Since the expiry of the core SHJ patents in the 2008–2010 period, multiple laboratories have rapidly demonstrated high-efficiency both-sides-contacted SHJ cells, as best exemplified by Kaneka.

Future challenges and opportunities

While the incorporation of passivating contacts has enabled considerable gains in record efficiencies in recent years, most of the passivating contact cell designs described above rely on processing schemes that considerably differ from the current industrial mainstream c-Si PV technology. This can be a significant roadblock towards rapid, large-scale industrial adoption. In this context, what is needed in the immediate future is a low-threshold upgrade of industrial c-Si PV manufacturing that only marginally affects existing production facilities, in order to minimize cost-of-ownership, learning, and re-tooling related risks. The most straightforward way to do so is by following the same philosophy that underlies the current shift from Al-BSF to PERC cells: address the recombination losses at the hole-collecting rear contacts in industrial silicon solar cells. For this, a simple hole-collecting passivating contact that can withstand the firing of screen printed metal contacts, as applied in industry, is currently sought after. To this end, p-type polysilicon or silicon-rich silicon carbide are promising material candidates, though issues related to the compatibility with conventional high temperature Ag screen print metallization still remain[84].

From a longer perspective, a shift in the cell production from p-type to n-type wafers is expected due to the higher tolerance of phosphorus-doped silicon to oxygen and common metallic impurities compared to boron-doped silicon[3]. This transition is likely to prompt greater adoption of passivating contact technologies both due to the departure from conventional p-type silicon solar cell processing procedures, especially the Al alloying process, and the increased benefit of passivating contacts on high bulk lifetime n-type wafers.

Further, as mentioned above, passivating contact technologies naturally provide greater flexibility in cell architecture. Full-area passivating contacts can easily be formed into bifacial designs where light is collected from both sides of the absorber, potentially improving the energy yield and thus lowering the levelized cost of energy for a given installation. The lower surface recombination also allows greater flexibility in the junction position. For example, an n-type rear junction cell with a front electron passivating contact can utilize a more resistive, but more transparent, TCO since the wafer can act as a lateral conductive channel for electrons[132]. Ultimately however, to meet the challenges faced by the increasing expansion of the PV industry towards terawatt-scale production[133], devices with passivating contacts featuring ITO may be threatened by the production scarcity, potential supply shocks, and ultimately, the relative lack of abundance of indium in the earth's crust[134]. Indium-free SHJ and equivalent cell architectures are therefore of great interest[135], and may be required if they are to meet predicted future market demand for PV. In addition, greatly reducing or eliminating Ag consumption in PV manufacturing is a general imperative for the c-Si community as a whole[133]. Beyond these potential constraints, the parasitic absorption in passivating contact devices can be further lowered by introducing wide bandgap metal oxides to replace the doped silicon ETLs (Fig. 5).

Alternatively, placing both passivating contacts at the rear-side of the device in an IBC configuration is arguably the ultimate cell design for high performance c-Si PV. However, to become an industrial reality, process and patterning simplification are of critical importance. Since passivating contact materials are typically fabricated by chemical or physical vapour deposition, or via solution processing, interesting new routes can be found to this end, enabling bottom-up concepts such as the tunnel-junction IBC cell[136]. Fully passivating contact c-Si technology is also anticipated to be the most attractive choice for the high-insolation, hot-climate market, as such cells feature the lowest temperature coefficient and so can result in higher energy yields[137].

Finally, to overcome the fast approaching 29.4% single-junction theoretical PCE limit of c-Si PV[4], passivating contact c-Si cells will arguably be the key driver as a bottom cell technology in a tandem cell configuration. This is thanks to the fact that such devices feature the highest operating voltages, even under reduced illumination conditions, such as in tandems; the passivating contacts can be tailored to provide excellent internal light reflection[138]; and the top cell filters out the short wavelength light, relaxing constraints on the bottom cell's blue response. In addition, the top contacts can easily be adapted into tunnel junctions, which are needed for monolithic 2-terminal tandem integration. This point has already been demonstrated using expensive III-V top cells, both for 4-terminal[139] and monolithic 2-terminal tandem cells[140]. For true industrial adoption it is likely that a cheaper top cell technology is needed. For this, perovskite solar cells, having excellent tuneable optoelectronic properties, are attractive candidates and have been integrated with c-Si bottom cells in both 2- and 4- terminal configurations, with rapidly improving efficiencies. In particular, most research groups working on the 2-terminal configuration have favoured the use of c-Si solar cells with passivating contacts due to the above described benefits[141,142].

Through the increasing trend towards passivating contacts, c-Si PV joins a larger group of optoelectronic devices that separate charge carriers via contact interfaces rather than with absorber doping. Many existing technologies, such as organic solar cells and light emitting diodes, which cannot easily implement functional impurity doping approaches, have already developed a suite of charge carrier selective contacts. Crystalline silicon stands to inherit knowledge from these fields, assisting to expedite the rapid uptake within mainstream PV. In addition, the accumulated knowledge relating to surface and contact passivation in c-Si can be of potential benefit to other material systems, as already demonstrated in CdTe[143] and CIGS devices[144]. Interestingly, highly efficient perovskite solar cells also increasingly feature passivating contacts, which prove to be effective in not only increasing the operating voltages, but also quenching the hysteresis effects in the current–voltage response[145,146]. For the mainstream c-Si PV industry, it is foreseeable that the physical constraints imposed by heavy doping will ultimately reshape the manufacturing landscape towards lost cost, high efficiency passivating contact solar cell designs, which will be a further driver towards the continued penetration of PVs into the global energy market.

Data availability

The data from plots in Figs. 1a,b, 3f,g, 5 and 6a are available in the Supplementary Data.

Received: 3 March 2019; Accepted: 8 August 2019;

References

1. *BP Statistical Review of World Energy*, June 2018 (BP, 2018).
2. Jager-Waldau, A. *PV Status Report 2018* (European Union, 2018).
3. *International Technology Roadmap for Photovoltaic (ITRPV) - Ninth Edition* (ITRPV, 2018).
4. Richter, A., Hermle, M. & Glunz, S. W. Reassessment of the limiting efficiency for crystalline silicon solar cells. *IEEE J. Photovolt.* **3**, 1184–1191 (2013).
5. Min, B. et al. A roadmap toward 24% efficient PERC solar cells in industrial mass production. *IEEE J. Photovolt.* **7**, 1541–1550 (2017).

6. Berney Needleman, D. et al. Economically sustainable scaling of photovoltaics to meet climate targets. *Energy Environ. Sci.* **9**, 2122–2129 (2016).
7. Basore, P. A. Paths to future growth in photovoltaics manufacturing. *Prog. Photovolt. Res. Appl.* **24**, 1024–1031 (2016).
8. Baker-Finch, S. C., McIntosh, K. R., Yan, D., Fong, K. C. & Kho, T. C. Near-infrared free carrier absorption in heavily doped silicon. *J. Appl. Phys.* **116**, 063106 (2014).
9. Yan, D. & Cuevas, A. Empirical determination of the energy band gap narrowing in highly doped n$^+$ silicon. *J. Appl. Phys.* **114**, 044508 (2013).
10. Yan, D. & Cuevas, A. Empirical determination of the energy band gap narrowing in p$^+$ silicon heavily doped with boron. *J. Appl. Phys.* **116**, 194505 (2014).
11. Richter, A., Glunz, S. W., Werner, F., Schmidt, J. & Cuevas, A. Improved quantitative description of Auger recombination in crystalline silicon. *Phys. Rev. B* **86**, (2012).
12. Green, M. A. The path to 25% silicon solar cell efficiency: history of silicon cell evolution. *Prog. Photovolt. Res. Appl.* **17**, 183–189 (2009).
    Outlines the historical development of silicon solar cells, with specific reference to the PERC cells that continue to hold the efficiency record for silicon devices with heavily doped, directly metallized contacts.
13. Zhao, J., Wang, A. & Green, M. A. 24·5% Efficiency silicon PERT cells on MCZ substrates and 24·7% efficiency PERL cells on FZ substrates. *Prog. Photovolt. Res. Appl.* **7**, 471–474 (1999).
14. Smith, D. D. et al. Toward the practical limits of silicon solar cells. *IEEE J. Photovolt.* **4**, 1465–1469 (2014).
15. Smith, D. D. et al. Silicon solar cells with total area efficiency above 25 %. In *Proc. IEEE 43rd Photovoltaic Specialists Conference (PVSC)* 3351–3355 (IEEE, 2016).
16. Adachi, D., Hernández, J. L. & Yamamoto, K. Impact of carrier recombination on fill factor for large area heterojunction crystalline silicon solar cell with 25.1% efficiency. *Appl. Phys. Lett.* **107**, 233506 (2015).
17. Masuko, K. et al. Achievement of more than 25% conversion efficiency with crystalline silicon heterojunction solar cell. *IEEE J. Photovolt.* **4**, 1433–1435 (2014).
18. Glunz, S. W. et al. The irresistible charm of a simple current flow pattern – 25% with a solar cell featuring a full-area back contact. In *Proc. 31st European Photovoltaic Solar Energy Conference and Exhibition* 259–263 (2015).
19. Richter, A. et al. n-Type Si solar cells with passivating electron contact: identifying sources for efficiency limitations by wafer thickness and resistivity variation. *Sol. Energy Mater. Sol. Cells* **173**, 96–105 (2017).
20. Yoshikawa, K. et al. Silicon heterojunction solar cell with interdigitated back contacts for a photoconversion efficiency over 26%. *Nat. Energy* **2**, 201732 (2017).
    Current world record efficiency for c-Si solar cells with an amorphous silicon SHJ passivating contact in an IBC configuration.
21. Green, M. A. et al. Solar cell efficiency tables (version 50). *Prog. Photovolt. Res. Appl.* **25**, 668–676 (2017).
22. Cuevas, A. & Macdonald, D. Measuring and interpreting the lifetime of silicon wafers. *Sol. Energy* **76**, 255–262 (2004).
23. Cuevas, A. The recombination parameter J$_0$. *Energy Procedia* **55**, 53–62 (2014).
24. Schmidt, J., Peibst, R. & Brendel, R. Surface passivation of crystalline silicon solar cells: present and future. *Sol. Energy Mater. Sol. Cells* **187**, 39–54 (2018).
25. Bonilla, R. S., Hoex, B., Hamer, P. & Wilshaw, P. R. Dielectric surface passivation for silicon solar cells: A review. *Phys. Status Solidi A* **214**, 1700293 (2017).
26. Tung, R. T. The physics and chemistry of the Schottky barrier height. *Appl. Phys. Rev.* **1**, 011304 (2014).
27. Schroder, D. K. & Meier, D. L. Solar cell contact resistance: a review. *IEEE Trans. Electron Devices* **31**, 637–647 (1984).
28. Melskens, J. et al. Passivating contacts for crystalline silicon solar cells: from concepts and materials to prospects. *IEEE J. Photovolt.* **8**, 373–388 (2018).
29. Glunz, S. W. & Feldmann, F. SiO$_2$ surface passivation layers—a key technology for silicon solar cells. *Sol. Energy Mater. Sol. Cells* **185**, 260–269 (2018).
30. Würfel, U., Cuevas, A. & Würfel, P. Charge carrier separation in solar cells. *IEEE J. Photovolt.* **5**, 461–469 (2015).
    Conceptual solar cell modelling demonstrating the physical basis by which contacts separate charge carriers in solar cells.
31. Cuevas, A. et al. Skin care for healthy silicon solar cells. In *Proc. IEEE 42nd Photovoltaic Specialist Conference (PVSC)* 1–6 (IEEE, 2015).
32. De Wolf, S., Descoeudres, A., Holman, Z. C. & Ballif, C. High-efficiency silicon heterojunction solar cells: a review. *Green* **2**, 7–24 (2012).
33. Würfel, P. *Physics of Solar Cells: From Principles to New Concepts* (Wiley, 2008).
34. Messmer, C., Bivour, M., Schön, J., Glunz, S. W. & Hermle, M. Numerical simulation of silicon heterojunction solar cells featuring metal oxides as carrier-selective contacts. *IEEE J. Photovolt.* **8**, 456–464 (2018).
35. Bullock, J. et al. Efficient silicon solar cells with dopant-free asymmetric heterocontacts. *Nat. Energy* **1**, 15031 (2016).
36. Green, M. A. & Godfrey, R. B. MIS silicon solar cells. *Jpn. J. Appl. Phys.* **17**, 295–298 (1978).
37. Battaglia, C. et al. Hole selective MoO$_x$ contact for silicon solar cells. *Nano Lett.* **14**, 967–971 (2014).
38. Allen, T. G. et al. Calcium contacts to n-type crystalline silicon solar cells. *Prog. Photovolt. Res. Appl.* **25**, 636–644 (2017).
39. Wolf, A. et al. Status and perspective of emitter formation by POCl$_3$-diffusion. In *Proc. 31st European Photovoltaic Solar Energy Conference and Exhibition* 414–419 (2015).
40. Lu, H., Guo, Y., Li, H. & Robertson, J. Modeling of surface gap state passivation and Fermi level de-pinning in solar cells. *Appl. Phys. Lett.* **114**, 222106 (2019).
41. Yablonovitch, E., Gmitter, T., Swanson, R. M. & Kwark, Y. H. A 720 mV open circuit voltage SiO$_x$:c-Si:SiO$_x$ double heterostructure solar cell. *Appl. Phys. Lett.* **47**, 1211–1213 (1985).
    Early demonstration of the surface passivation potential of doped poly-silicon or SIPOS-based contacts, which would form the basis of extensive recent research, for example in so-called TOPCon contacts.
42. Liu, Y., Stradins, P., Deng, H., Luo, J. & Wei, S.-H. Suppress carrier recombination by introducing defects: the case of Si solar cell. *Appl. Phys. Lett.* **108**, 022101 (2016).
43. Brendel, R. & Peibst, R. Contact selectivity and efficiency in crystalline silicon photovoltaics. *IEEE J. Photovolt.* **6**, 1413–1420 (2016).
44. MacDonald, D., Cuevas, A., McIntosh, K., Barbosa, L. & De Ceuster, D. Impact of Cr, Fe, Ni, Ti and W surface contamination on diffused and oxidised a-type crystalline silicon wafers. In *Proc. 20th European Photovoltaic Solar Energy Conference* 1–4 (WIP Renewable Energies, 2005).
45. Nagamatsu, K. A. et al. Titanium dioxide/silicon hole-blocking selective contact to enable double-heterojunction crystalline silicon-based solar cell. *Appl. Phys. Lett.* **106**, 123906 (2015).
46. Ponpon, J. P. & Siffert, P. Open-circuit voltage of MIS silicon solar cells. *J. Appl. Phys.* **47**, 3248–3251 (1976).
47. Tarr, N. G., Pulfrey, D. L. & Iles, P. A. Induced back-surface field solar cells on p-type silicon substrates. *Appl. Phys. Lett.* **39**, 83–85 (1981).
48. Godfrey, R. B. & Green, M. A. High-efficiency silicon minMIS solar cells—design and experimental results. *IEEE Trans. Electron Devices* **27**, 737–745 (1980).
49. Godfrey, R. B. & Green, M. A. 655 mV open-circuit voltage, 17.6% efficient silicon MIS solar cells. *Appl. Phys. Lett.* **34**, 790–793 (1979).
    Early demonstration of an archetypal silicon passivating contact solar cell using a thin silicon oxide layer to separate the absorber material from the metal contact, resulting in a record open circuit voltage at the time of publication.
50. Hezel, R. Recent progress in MIS solar cells. *Prog. Photovolt. Res. Appl.* **5**, 109–120 (1997).
51. Hezel, R. Plasma Si nitride—a promising dielectric to achieve high-quality silicon MIS/IL solar cells. *J. Appl. Phys.* **52**, 3076 (1981).
52. Jager, K. & Hezel, R. Optical stability of silicon nitride MIS inversion layer solar cells. *IEEE Trans. Electron Devices* **32**, 1824–1829 (1985).
53. Metz, A., Meyer, R., Kuhlmann, B., Grauvogl, M. & Hezel, R. 18.5% efficient first-generation MIS inversion-layer silicon solar cells. In *Proc. Conference Record of the 26th IEEE Photovoltaic Specialists Conference* 31–34 (IEEE, 1997).
54. Hezel, R., Meyer, R. & Metz, A. A new generation of crystalline silicon solar cells: simple processing and record efficiencies for industrial-size devices. *Sol. Energy Mater.* **6** (2001).
55. Blakers, A. W. & Green, M. A. 678-mV open-circuit voltage silicon solar cells. *Appl. Phys. Lett.* **39**, 483–485 (1981).
56. Blakers, A. W. et al. 18-percent efficient terrestrial silicon solar cells. *IEEE Electron Device Lett.* **5**, 12–13 (1984).
57. Zielke, D. et al. Contact passivation in silicon solar cells using atomic-layer-deposited aluminum oxide layers. *Phys. Status Solidi RRL—Rapid Res. Lett.* **5**, 298–300 (2011).
58. Bullock, J. et al. Amorphous silicon enhanced metal-insulator-semiconductor contacts for silicon solar cells. *J. Appl. Phys.* **116**, 163706 (2014).
59. Bullock, J. et al. Simple silicon solar cells featuring an a-Si:H enhanced rear MIS contact. *Sol. Energy Mater. Sol. Cells* **138**, 22–25 (2015).
60. Tarr, N. G. A polysilicon emitter solar cell. *IEEE Electron Device Lett.* **6**, 655–658 (1985).
61. Kwark, Y. H. & Swanson, R. M. N-type SIPOS and poly-silicon emitters. *Solid-State Electron.* **30**, 1121–1125 (1987).
62. Kwark, Y. H., Sinton, R. & Swanson, R. M. SIPOS Heterojunction contacts to silicon. In *Proc. 1984 International Electron Devices Meeting* 742–745 (IEEE, 1984).

63. Post, I. R. C., Ashburn, P. & Wolstenholme, G. R. Polysilicon emitters for bipolar transistors: a review and re-evaluation of theory and experiment. *IEEE Trans. Electron Devices* **39**, 1717–1731 (1992).
64. Gan, J. Y. & Swanson, R. M. Polysilicon emitters for silicon concentrator solar cells. In *Proc. IEEE Conference on Photovoltaic Specialists* 245–250 (IEEE, 1990).
65. Tetzlaff, D. et al. A simple method for pinhole detection in carrier selective POLO-junctions for high efficiency silicon solar cells. *Sol. Energy Mater. Sol. Cells* **173**, 106–110 (2017).
66. Peibst, R. et al. Working principle of carrier selective poly-Si/c-Si junctions: is tunnelling the whole story? *Sol. Energy Mater. Sol. Cells* **158**, 60–67 (2016).
67. Feldmann, F. et al. Charge carrier transport mechanisms of passivating contacts studied by temperature-dependent J-V measurements. *Sol. Energy Mater. Sol. Cells* **178**, 15–19 (2018).
68. Mack, S. et al. Metallisation of boron-doped polysilicon layers by screen printed silver pastes. *Phys. Status Solidi Rapid Res. Lett.* **11**, 1700334 (2017).
69. Rienäcker, M. et al. Junction resistivity of carrier-selective polysilicon on oxide junctions and its impact on solar cell performance. *IEEE J. Photovolt.* **7**, 1–8 (2016).
70. Larionova, Y. et al. On the recombination behavior of p^+-type polysilicon on oxide junctions deposited by different methods on textured and planar surfaces. *Phys. Status Solidi A* **214**, 1700058 (2017).
71. Hollemann, C. et al. 26.1%-efficient POLO-IBC cells: quantification of electrical and optical loss mechanisms. *Prog. Photovolt. Res. Appl.* 1–9 (2019).
72. Okuda, K., Okamoto, H. & Hamakawa, Y. Amorphous Si/polycrystalline Si stacked solar cell having more than 12% conversion efficiency. *Jpn. J. Appl. Phys.* **22**, L605 (1983).
73. Pankove, J. I. & Tarng, M. L. Amorphous silicon as a passivant for crystalline silicon. *Appl. Phys. Lett.* **34**, 156–157 (1979).
74. Taguchi, M. et al. Improvement of the conversion efficiency of polycrystalline silicon thin film solar cell. In *Proc. Technical Digest of the International PVSEC-5, Kyoto, Japan* 689–692 (1990).
Initial demonstration of a-Si-based heterojunction contacts to c-Si, initially for application in a-Si/poly-Si tandem cells, which would form the basis of the silicon heterojunction (SHJ) device architecture.
75. Taguchi, M. et al. HIT cells—high-efficiency crystalline Si cells with novel structure. *Prog. Photovolt. Res. Appl.* **8**, 503–513 (2000).
76. Nogay, G. et al. Nanocrystalline silicon carrier collectors for silicon heterojunction solar cells and impact on low-temperature device characteristics. *IEEE J. Photovolt.* **6**, 1654–1662 (2016).
77. Schulze, T. F., Korte, L., Conrad, E., Schmidt, M. & Rech, B. Electrical transport mechanisms in a-Si:H/c-Si heterojunction solar cells. *J. Appl. Phys.* **107**, 023711 (2010).
78. Tomasi, A. et al. Transparent electrodes in silicon heterojunction solar cells: influence on contact passivation. *IEEE J. Photovolt.* **6**, 17–27 (2016).
79. Procel, P., Yang, G., Isabella, O. & Zeman, M. Theoretical evaluation of contact stack for high efficiency IBC-SHJ solar cells. *Sol. Energy Mater. Sol. Cells* **186**, 66–77 (2018).
80. Holman, Z. C. et al. Current losses at the front of silicon heterojunction solar cells. *IEEE J. Photovolt.* **2**, 7–15 (2012).
81. Taguchi, M. et al. 24.7% record efficiency hit solar cell on thin silicon wafer. *IEEE J. Photovolt.* **4**, 96–99 (2014).
82. Seif, J. P. et al. Amorphous silicon oxide window layers for high-efficiency silicon heterojunction solar cells. *J. Appl. Phys.* **115**, 024502 (2014).
83. Boccard, M. & Holman, Z. C. Amorphous silicon carbide passivating layers for crystalline-silicon-based heterojunction solar cells. *J. Appl. Phys.* **118**, 065704 (2015).
84. Ingenito, A. et al. A passivating contact for silicon solar cells formed during a single firing thermal annealing. *Nat. Energy* **3**, 800 (2018).
85. Wernerus, H., Bivour, M., Kroely, L., Hermle, M. & Wolke, W. Characterization of ultra-thin μc-Si:H films for silicon heterojunction solar cells. *Energy Procedia* **55**, 310–319 (2014).
86. Mazzarella, L. et al. p-type microcrystalline silicon oxide emitter for silicon heterojunction solar cells allowing current densities above 40 mA/cm^2. *Appl. Phys. Lett.* **106**, 023902 (2015).
87. Morales-Masis, M., De Wolf, S., Woods-Robinson, R., Ager, J. W. & Ballif, C. Transparent electrodes for efficient optoelectronics. *Adv. Electron. Mater.* **3**, 1600529 (2017).
88. Yang, X. et al. High-performance TiO_2-based electron-selective contacts for crystalline silicon solar cells. *Adv. Mater.* **28**, 5891–5897 (2016).
89. Allen, T. G. et al. A low resistance calcium/reduced titania passivated contact for high efficiency crystalline silicon solar cells. *Adv. Energy Mater.* **7**, 1602606 (2017).
90. Macco, B. et al. Atomic-layer deposited Nb_2O_5 as transparent passivating electron contact for c-Si solar cells. *Sol. Energy Mater. Sol. Cells* **184**, 98–104 (2018).
91. Wan, Y., Bullock, J. & Cuevas, A. Passivation of c-Si surfaces by ALD tantalum oxide capped with PECVD silicon nitride. *Sol. Energy Mater. Sol. Cells* **142**, 42–46 (2015).
92. Allen, T. G. & Cuevas, A. Electronic passivation of silicon surfaces by thin films of atomic layer deposited gallium oxide. *Appl. Phys. Lett.* **105**, 031601 (2014).
93. Smit, S., Garcia-Alonso, D., Bordihn, S., Hanssen, M. S. & Kessels, W. M. M. Metal-oxide-based hole-selective tunneling contacts for crystalline silicon solar cells. *Sol. Energy Mater. Sol. Cells* **120**, 376–382 (2014).
94. Zhang, Y. et al. High efficiency hybrid PEDOT:PSS/nanostructured silicon Schottky junction solar cells by doping-free rear contact. *Energy Environ. Sci.* **8**, 297–302 (2014).
95. Shewchun, J., Burk, D. & Spitzer, M. B. MIS and SIS solar cells. *IEEE Trans. Electron Devices* **27**, 705–716 (1980).
96. Ghosh, A. K., Fishman, C. & Feng, T. SnO_2 /Si solar cells—heterostructure or Schottky-barrier or MIS-type device. *J. Appl. Phys.* **49**, 3490–3498 (1978).
97. Yang, X., Weber, K., Hameiri, Z. & De Wolf, S. Industrially feasible, dopant-free, carrier-selective contacts for high-efficiency silicon solar cells. *Prog. Photovolt. Res. Appl.* **25**, 896–904 (2017).
98. Bullock, J. et al. Dopant-free partial rear contacts enabling 23% silicon solar cells. *Adv. Energy Mater.* **9**, 1803367 (2019).
99. Zhang, X., Wan, Y., Bullock, J., Allen, T. & Cuevas, A. Low resistance Ohmic contact to p-type crystalline silicon via nitrogen-doped copper oxide films. *Appl. Phys. Lett.* **109**, 052102 (2016).
100. Battaglia, C. et al. Silicon heterojunction solar cell with passivated hole selective MoO_x contact. *Appl. Phys. Lett.* **104**, 113902 (2014).
Exemplary dopant-free hole contact—common in organic electronics—applied to silicon, spurring further research into MoO_x and other high/low work function, dopant free materials, including other transition metal oxides.
101. Bullock, J., Cuevas, A., Allen, T. & Battaglia, C. Molybdenum oxide MoO_x: A versatile hole contact for silicon solar cells. *Appl. Phys. Lett.* **105**, 232109 (2014).
102. Bivour, M., Temmler, J., Steinkemper, H. & Hermle, M. Molybdenum and tungsten oxide: high work function wide band gap contact materials for hole selective contacts of silicon solar cells. *Sol. Energy Mater. Sol. Cells* **142**, 34–41 (2015).
103. Gerling, L. G. et al. Transition metal oxides as hole-selective contacts in silicon heterojunctions solar cells. *Sol. Energy Mater. Sol. Cells* **145**, 109–115 (2016).
104. Meyer, J. et al. Transition metal oxides for organic electronics: energetics, device physics and applications. *Adv. Mater.* **24**, 5408–5427 (2012).
105. Bullock, J. et al. Proof-of-concept p-type silicon solar cells with molybdenum oxide local rear contacts. *IEEE J. Photovolt.* **5**, 1591–1594 (2015).
106. Xu, X. et al. Chemical bath deposition of p-type transparent, highly conducting $(CuS)_x$:$(ZnS)_{1-x}$ nanocomposite thin films and fabrication of Si heterojunction solar cells. *Nano Lett.* **16**, 1925–1932 (2016).
107. Yang, X. et al. Tantalum nitride electron-selective contact for crystalline silicon solar cells. *Adv. Energy Mater.* **8**, 1800608 (2018).
108. Yang, X. et al. Dual-function electron-conductive, hole-blocking titanium nitride contacts for efficient silicon solar cells. *Joule* **3**, 1314–1327 (2019).
109. Feifel, M. et al. MOVPE grown gallium phosphide-silicon heterojunction solar cells. *IEEE J. Photovolt.* **7**, 502–507 (2017).
110. He, J. et al. High-efficiency silicon/organic heterojunction solar cells with improved junction quality and interface passivation. *ACS Nano* **10**, 11525–11531 (2016).
111. Wan, Y. et al. Temperature and humidity stable alkali/alkaline-earth metal carbonates as electron heterocontacts for silicon photovoltaics. *Adv. Energy Mater.* **8**, 1800743 (2018).
112. Ishii, H., Sugiyama, K., Ito, E. & Seki, K. Energy level alignment and interfacial electronic structures at organic/metal and organic/organic interfaces. *Adv. Mater.* **11**, 605–625 (1999).
113. Bullock, J. et al. Lithium fluoride based electron contacts for high efficiency n-type crystalline silicon solar cells. *Adv. Energy Mater*. **6**, (2016).
114. Coss, B. E. et al. Near band edge Schottky barrier height modulation using high-κ dielectric dipole tuning mechanism. *Appl. Phys. Lett.* **95**, 222105 (2009).
115. Lacharme, J. P., Benazzi, N. & Sébenne, C. A. Compositional and electronic properties of Si(001)2×1 upon diatomic sulfur interaction. *Surf. Sci.* **433**, 415–419 (1999).
116. Zhang, X. et al. High-efficiency graphene/Si nanoarray Schottky junction solar cells via surface modification and graphene doping. *J. Mater. Chem. A* **1**, 6593–6601 (2013).
117. Tune, D. D., Flavel, B. S., Krupke, R. & Shapter, J. G. Carbon nanotube-silicon solar cells. *Adv. Energy Mater.* **2**, 1043–1055 (2012).
118. Tsai, M.-L. et al. Monolayer MoS_2 heterojunction solar cells. *ACS Nano* **8**, 8317–8322 (2014).
119. Wang, D. et al. Tuning back contact property via artificial interface dipoles in Si/organic hybrid solar cells. *Appl. Phys. Lett.* **109**, 043901 (2016).
120. Zhang, Y. et al. Heterojunction with organic thin layers on silicon for record efficiency hybrid solar cells. *Adv. Energy Mater.* **4**, 1300923 (2014).

121. Reichel, C. et al. Electron-selective contacts via ultra-thin organic interface dipoles for silicon organic heterojunction solar cells. *J. Appl. Phys.* **123**, 024505 (2018).
122. Zielke, D. et al. Organic-silicon solar cells exceeding 20% efficiency. *Energy Procedia* **77**, 331–339 (2015).
123. He, L., Jiang, C., Rusli, Lai, D. & Wang, H. Highly efficient Si-nanorods/organic hybrid core-sheath heterojunction solar cells. *Appl. Phys. Lett.* **99**, 021104 (2011).
124. Zielke, D. et al. Large-area PEDOT:PSS/c-Si heterojunction solar cells with screen-printed metal contacts. *Sol. RRL* **2**, 1700191 (2018).
125. Gogolin, R. et al. Demonstrating the high Voc potential of PEDOT:PSS/c-Si heterojunctions on solar cells. *Energy Procedia* **124**, 593–597 (2017).
126. Liu, R., Lee, S.-T. & Sun, B. 13.8% Efficiency hybrid Si/organic heterojunction solar cells with MoO_3 film as antireflection and inversion induced layer. *Adv. Mater.* **26**, 6007–6012 (2014).
127. Bullock, J. et al. Stable dopant-free asymmetric heterocontact silicon solar cells with efficiencies above 20%. *ACS Energy Lett.* **3**, 508–513 (2018).
128. Um, H.-D. et al. Dopant-free all-back-contact Si nanohole solar cells using MoO_x and LiF Films. *Nano Lett.* **16**, 981–987 (2016).
129. Wu, W. et al. 22% efficient dopant-free interdigitated back contact silicon solar cells. *AIP Conf. Proc.* **1999**, 040025 (2018).
130. Yoshikawa, K. et al. Exceeding conversion efficiency of 26% by heterojunction interdigitated back contact solar cell with thin film Si technology. *Sol. Energy Mater. Sol. Cells* **173**, 37–42 (2017).
131. Altermatt, P. P. et al. Learning from the past to look beyond the roadmap of PERC Si solar cell mass production. In *Proc. 35th European Photovoltaic Solar Energy Conference and Exhibition* 1–7 (2018).
132. Bivour, M., Reichel, C., Hermle, M. & Glunz, S. W. Improving the a-Si:H(p) rear emitter contact of n-type silicon solar cells. *Sol. Energy Mater. Sol. Cells* **106**, 11–16 (2012).
133. Davidsson, S. & Höök, M. Material requirements and availability for multi-terawatt deployment of photovoltaics. *Energy Policy* **108**, 574–582 (2017).
134. Kavlak, G., McNerney, J., Jaffe, R. L. & Trancik, J. E. Metal production requirements for rapid photovoltaics deployment. *Energy Environ. Sci.* **8**, 1651–1659 (2015).
135. Morales-Vilches, A. B. et al. ITO-free silicon heterojunction solar cells with ZnO:Al/SiO_2 front electrodes reaching a conversion efficiency of 23%. *IEEE J. Photovolt.* **9**, 34–39 (2019).
136. Tomasi, A. et al. Simple processing of back-contacted silicon heterojunction solar cells using selective-area crystalline growth. *Nat. Energy* **2**, 17062 (2017).
137. Haschke, J. et al. The impact of silicon solar cell architecture and cell interconnection on energy yield in hot & sunny climates. *Energy Environ. Sci.* **10**, 1196–1206 (2017).
138. Holman, Z. C., Descoeudres, A., De Wolf, S. & Ballif, C. Record infrared internal quantum efficiency in silicon heterojunction solar cells with dielectric/metal rear reflectors. *IEEE J. Photovolt.* **3**, 1243–1249 (2013).
139. Essig, S. et al. Raising the one-sun conversion efficiency of III–V/Si solar cells to 32.8% for two junctions and 35.9% for three junctions. *Nat. Energy* **2**, 17144 (2017).
140. Cariou, R. et al. III-V-on-silicon solar cells reaching 33% photoconversion efficiency in two-terminal configuration. *Nat. Energy* **3**, 326–333 (2018).
141. Bush, K. A. et al. 23.6%-efficient monolithic perovskite/silicon tandem solar cells with improved stability. *Nat. Energy* **2**, 17009 (2017).
142. Sahli, F. et al. Fully textured monolithic perovskite/silicon tandem solar cells with 25.2% power conversion efficiency. *Nat. Mater.* **17**, 820 (2018).
143. Zhao, Y. et al. Monocrystalline CdTe solar cells with open-circuit voltage over 1 V and efficiency of 17%. *Nat. Energy* **1**, 16067 (2016).
144. Vermang, B. et al. Employing Si solar cell technology to increase efficiency of ultra-thin Cu(In, Ga)Se_2 solar cells. *Prog. Photovolt. Res. Appl.* **22**, 1023–1029 (2014).
145. Tan, H. et al. Efficient and stable solution-processed planar perovskite solar cells via contact passivation. *Science* **355**, 722–726 (2017).
146. Peng, J. et al. Interface passivation using ultrathin polymer–fullerene films for high-efficiency perovskite solar cells with negligible hysteresis. *Energy Environ. Sci.* **10**, 1792–1800 (2017).
147. Young, R. T., van der Leeden, G. A., Sandstrom, R. L., Wood, R. F. & Westbrook, R. D. High-efficiency Si solar cells by beam processing. *Appl. Phys. Lett.* **43**, 666–668 (1983).
148. Mulligan, W. P. & Swanson, R. M. High efficiency, one-sun solar cell processing. In *Proc. 13th NREL Workshop on Crystalline Silicon Solar Cell Materials and Processes: Extended Abstracts and Papers* (Ed. Sopori, B. L.) 30–37 (NREL, 2003).
149. Mulligan, W. P. et al. Manufacture of solar cells with 21% efficiency. In *Proc.19th European Photovoltaic Solar Energy Conference* 1–4 (2004).
150. Green, M. A., Emery, K., King, D. L., Hishikawa, Y. & Warta, W. Solar cell efficiency tables (version 28). *Prog. Photovolt. Res. Appl.* **14**, 455–461 (2006).
151. Cousins, P. J. et al. Generation 3: improved performance at lower cost. In *Proc. 35th IEEE Photovoltaic Specialists Conference* 275–278 (IEEE, 2010).
152. Green, M. A., Emery, K., Hishikawa, Y., Warta, W. & Dunlop, E. D. Solar cell efficiency tables (version 44). *Prog. Photovolt. Res. Appl.* **22**, 701–710 (2014).
153. Tanaka, M. et al. Development of new a-Si/c-Si heterojunction solar cells: ACJ-HIT (artificially constructed junction-heterojunction with intrinsic thin-layer). *Jpn. J. Appl. Phys.* **31**, 3518 (1992).
154. Sawada, T. et al. High-efficiency a-Si/c-Si heterojunction solar cell. In *Proc. 1994 IEEE 1st World Conference on Photovoltaic Energy Conversion - WCPEC (A Joint Conference of PVSC, PVSEC and PSEC)* 1219–1226 (IEEE, 1994).
155. Taguchi, M. et al. An approach for the higher efficiency in the HIT cells. In *Conference Record of the Thirty-first IEEE Photovoltaic Specialists Conference* 866–871 (IEEE, 2005).
156. Sakata, H. et al. 20.7% highest efficiency large area (100.5 cm^2) HIT/TM/cell. In *Conference Record of the 28th IEEE Photovoltaic Specialists Conference* 7–12 (IEEE, 2000).
157. Taguchi, M. et al. High-Efficiency HIT Solar Cell on Thin (<100 µm) Silicon Wafer. In *24th European Photovoltaic Solar Energy Conference* 1690–1693 (2009).
158. Dullweber, T. & Schmidt, J. Industrial silicon solar cells applying the passivated emitter and rear cell (PERC) concept:a review. *IEEE J. Photovolt.* **6**, 1366–1381 (2016).
159. Gatz, S. et al. 19.4%-efficient large-area fully screen-printed silicon solar cells. *Phys. Status Solidi RRL – Rapid Res. Lett.* **5**, 147–149 (2011).
160. Metz, A. et al. Industrial high performance crystalline silicon solar cells and modules based on rear surface passivation technology. *Sol. Energy Mater. Sol. Cells* **120**, 417–425 (2014).
161. Colthorpe, A. SolarWorld touts 21.7% PERC world record efficiency. *PV Tech* https://www.pv-tech.org/news/solarworld_touts_21.7_perc_world_record_efficiecny (2015)
162. Ye, F. et al. 22.13% Efficient industrial p-type mono PERC solar cell. In *Proc. 2016 IEEE 43rd Photovoltaic Specialists Conference (PVSC)* 3360–3365 (IEEE, 2016).
163. Weiwei, D. et al. 22.61% efficient fully screen printed perc solar cell. In *IEEE 44th Photovoltaic Specialist Conference (PVSC)* (2017).
164. Trina Solar sets new 22.61% mono PERC efficiency record. *pv magazine* https://www.pv-magazine.com/2016/12/19/trina-solar-sets-new-22-61-mono-perc-efficiency-record/ (2016)
165. JinkoSolar claims new 22. 78% PERC efficiency record. *pv magazine* https://www.pv-magazine.com/2017/10/25/jinkosolar-claims-new-22-78-perc-efficiency-record (2017)
166. Parnell, J. Jinko beats its own mono PERC efficiency record. *PV Tech* https://www.pv-tech.org/news/jinko-beats-its-own-mono-perc-efficiency-record (2017)
167. Kenning, T. LONGi hits record 23.6% conversion efficiency for mono PERC solar cells. *PV Tech* https://www.pv-tech.org/news/longi-hits-record-23.6-conversion-efficiency-for-mono-perc-solar-cells (2018)
168. Feldmann, F., Bivour, M., Reichel, C., Hermle, M. & Glunz, S. W. Passivated rear contacts for high-efficiency n-type Si solar cells providing high interface passivation quality and excellent transport characteristics. *Sol. Energy Mater. Sol. Cells* **120**, 270–274 (2014).
169. Feldmann, F., Reichel, M. B. C., Hermle, M. & Glunz, S. W. A passivated rear contact for high efficiency n-type silicon solar cells enabling high V_{oc}s and FF > 82%. In *Proc. 28th European Photovoltaic Solar Energy Conference and Exhibition* (2013).
170. Feldmann, F. et al. Tunnel oxide passivated contacts as an alternative to partial rear contacts. *Sol. Energy Mater. Sol. Cells* **131**, 46–50 (2014).
171. Rienäcker, M. et al. Recombination behavior of photolithography-free back junction back contact solar cells with carrier-selective polysilicon on oxide junctions for both polarities. *Energy Procedia* **92**, 412–418 (2016).
172. Haase, F. et al. Interdigitated back contact solar cells with polycrystalline silicon on oxide passivating contacts for both polarities. *Jpn. J. Appl. Phys.* **56**, (2017).
173. Hernández, J. L. et al. High efficiency silver-free heterojunction silicon solar cell. *Jpn. J. Appl. Phys.* **51**, (2012).
174. Hernández, J. L. et al. High efficiency copper electroplated heterojunction solar cells. In *Proc. 27th European Photovoltaic Solar Energy Conference and Exhibition* 655–656 (WIP Renewable Energies, 2012).
175. Yamamoto, K. et al. High-efficiency heterojunction crystalline Si solar cell and optical splitting structure fabricated by applying thin-film Si technology. *Jpn. J. Appl. Phys.* **54**, (2015).
176. Green, M. A. et al. Solar cell efficiency tables (version 49): Solar cell efficiency tables (version 49). *Prog. Photovolt. Res. Appl.* **25**, 3–13 (2017).
177. Blakers, A. W. & Green, M. A. 20% efficiency silicon solar cells. *Appl. Phys. Lett.* **48**, 215–217 (1986).
178. Blakers, A. W., Wang, A., Milne, A. M., Zhao, J. & Green, M. A. 22.8% efficient silicon solar cell. *Appl. Phys. Lett.* **55**, 1363–1365 (1989).
179. Green, M. A. et al. Characterization of 23-percent efficient silicon solar cells. *IEEE Trans. Electron Devices* **37**, 331–336 (1990).

180. Zhao, J., Wang, A. & Green, M. A. 24% efficient PERL structure silicon solar cells. In *Proc. IEEE Conference on Photovoltaic Specialists* 333–335 (IEEE, 1990).
181. Zhang, S. et al. 335-W World-Record p-Type Monocrystalline Module With 20.6% Efficient PERC Solar Cells. *IEEE J. Photovolt.* **6**, 145–152 (2016).
182. Tsunomura, Y. et al. Twenty-two percent efficiency HIT solar cell. *Sol. Energy Mater. Sol. Cells* **93**, 670–673 (2009).
183. Mishima, T., Taguchi, M., Sakata, H. & Maruyama, E. Development status of high-efficiency HIT solar cells. *Sol. Energy Mater. Sol. Cells* **95**, 18–21 (2011).
184. Green, M. A. Solar cell fill factors: General graph and empirical expressions. *Solid-State Electron.* **24**, 788–789 (1981).
185. Plagwitz, H., Nerding, M., Ott, N., Strunk, H. P. & Brendel, R. Low-temperature formation of local Al contacts to a-Si:H-passivated Si wafers. *Prog. Photovolt. Res. Appl.* **12**, 47–54 (2004).
186. H. Plagwitz. et al. 20%-efficient silicon solar cells with local contacts to the a-Si-passivated surfaces by means of annealing (COSIMA). In *Proc. 20th European Photovoltaic Solar Energy Conference and Exhibition* 725–728 (WIP Renewable Energies, 2005).
187. Heinemeyer, F., Mader, C., Münster, D., Dullweber, T. & Brendel, R. Inline high-rate thermal evaporation of aluminum for novel industrial solar cell metallization. In *Proc. 25th European Photovoltaic Solar Energy Conference Conversion* (WIP Renewable Energies, 2010).
188. Mader, C., Müller, J., Eidelloth, S. & Brendel, R. Local rear contacts to silicon solar cells by in-line high-rate evaporation of aluminum. *Sol. Energy Mater. Sol. Cells* **107**, 272–282 (2012).
189. Rohatigi, A., Narasimha, S. & Ruby, D. S. Effective passivation of the low resistivity silicon surface by a rapid thermal oxide/PECVD silicon nitride stack and application to passivated rear and bifacial Si solar cells. In *Proc. 2nd World Conference and Exhibition on Photovoltaic Solar Energy Conversion, Vienna, Austria* (Georgia Institute of Technology, 1998).
190. Riegel, S., Mutter, F., Hahn, G. & Terheiden, B. Influence of the dopant on the contact formation to p^+-type silicon. *Energy Procedia* **8**, 533–539 (2011).
191. Urrejola, E., Peter, K., Plagwitz, H. & Schubert, G. Al–Si alloy formation in narrow p-type Si contact areas for rear passivated solar cells. *J. Appl. Phys.* **107**, 124516 (2010).
192. Gatz, S., Dullweber, T. & Brendel, R. Evaluation of series resistance losses in screen-printed solar cells with local rear contacts. *IEEE J. Photovolt.* **1**, 37–42 (2011).
193. Richter, A., Hörteis, M., Benick, J., Hermle, M. & Glunz, S. W. Seed layer printed contact formation for highly doped boron emitters of n-type silicon solar cells with front side junction. In *Proc. 2nd Workshop on Metallization for Crystalline Silicon Solar Cells* 26–31 (2010).
194. Seren, S., Braun, S., Schiele, Y., Hahn, G. & Terheiden, B. Nickel plating on p^+ silicon - a characterization of contact resistivity and line resistance. In *Proc. 27th European Photovoltaic Solar Energy Conference and Exhibition* 1777–1780 (WIP Renewable Energies, 2012).
195. Binder, S., Bartsch, J., Glatthaar, M. & Glunz, S. Printed contact on emitter with low dopant surface concentration. *Energy Procedia* **21**, 32–38 (2012).
196. Hörteis, M. *Fine-line Printed Contacts on Crystalline Silicon Solar Cells*. PhD thesis, University of Konstanz (2009).
197. Mette, A. *New Concepts for Front Side Metallization of Industrial Silicon Solar Cells*. PhD thesis, Albert-Ludwigs Univ. (2007).
198. Gunnar, S. *Thick Film Metallisation of Crystalline Silicon Solar Cells: Mechanisms, Models and Applications*. PhD thesis, University of Konstanz (2006).
199. Vinod, P. N. Specific contact resistance measurement of screen-printed ag metal contacts formed on heavily doped emitter region in multicrystalline silicon solar cells. *J. Electron. Mater.* **42**, 2905–2909 (2013).
200. Braun, S., Emre, E., Raabe, B. & Hahn, G. Electroless nickel and copper metallization: Contact formation on crystalline silicon and background plating behavior on PECVD silicon SiN_x:H layers. In *Proc. 25th European Photovoltaic Solar Energy Conference and Exhibition/5th World Conference on photovoltaic Energy Conversion* 1892–1895 (WIP Renewable Energies, 2010).
201. Rauer, M. et al. Nickel-plated front contacts for front and rear emitter silicon solar cells. *Energy Procedia* **38**, 449–458 (2013).
202. Richter, A. et al. Towards industrial n-type PERT silicon solar cells: rear passivation and metallization scheme. *Energy Procedia* **8**, 479–486 (2011).
203. Woehl, R. et al. Evaluating the aluminum-alloyed p^+-layer of silicon solar cells by emitter saturation current density and optical microspectroscopy measurements. *IEEE Trans. Electron Devices* **58**, 441–447 (2011).
204. Bullock, J. *Advanced Contacts for Silicon Solar Cells*. PhD thesis, The Australian National Univ. (2016).
205. Cuevas, A., Basore, P. A., Giroult-Matlakowski, G. & Dubois, C. Surface recombination velocity of highly doped n-type silicon. *J. Appl. Phys.* **80**, 3370–3375 (1996).
206. Kerr, M. J. *Surface, Emitter and Bulk Recombination in Silicon and Development of Silicon Nitride Passivated Solar Cells*. PhD thesis, The Australian National Univ. (2002).
207. Sze, S. M. & Ng, K. K. *Physics of Semiconductor Devices* 3rd edn (John Wiley & Sons, 2006).
208. McIntosh, K. R. & Altermatt, P. P. A freeware 1D emitter model for silicon solar cells. In *Proc. 35th IEEE Photovoltaic Specialists Conference (PVSC)* 002188–002193 (IEEE, 2010).
209. EDNA 2. *PV Lighthouse* https://www2.pvlighthouse.com.au/calculators/EDNA%202/EDNA%202.aspx (2018)
210. Luo, W. et al. Copper thiocyanate/copper iodide based hole transport composites with balanced properties for efficient polymer light-emitting diodes. *J. Mater. Chem. C.* **6**, 4895–4902 (2018).
211. Zhao, K. et al. Solution-processed inorganic copper(i) thiocyanate (CuSCN) hole transporting layers for efficient p-i-n perovskite solar cells. *J. Mater. Chem. A* **3**, 20554–20559 (2015).
212. Steirer, K. X. et al. Solution deposited NiO thin-films as hole transport layers in organic photovoltaics. *Org. Electron.* **11**, 1414–1418 (2010).
213. Chen, T.-G., Huang, B.-Y., Chen, E.-C., Yu, P. & Meng, H.-F. Micro-textured conductive polymer/silicon heterojunction photovoltaic devices with high efficiency. *Appl. Phys. Lett.* **101**, 033301 (2012).
214. Meyer, B. K. et al. Binary copper oxide semiconductors: From materials towards devices. *Phys. Status Solidi B* **249**, 1487–1509 (2012).
215. Tanaka, Y., Kanai, K., Ouchi, Y. & Seki, K. Oxygen effect on the interfacial electronic structure of C_{60} film studied by ultraviolet photoelectron spectroscopy. *Chem. Phys. Lett.* **441**, 63–67 (2007).
216. Hu, C. et al. Work function variation of monolayer MoS_2 by nitrogen-doping. *Appl. Phys. Lett.* **113**, 041602 (2018).
217. Jiang, Q. et al. Enhanced electron extraction using SnO_2 for high-efficiency planar-structure $HC(NH_2)_2PbI_3$-based perovskite solar cells. *Nat. Energy* **2**, 16177 (2017).
218. Ling, X. et al. Room-temperature processed Nb_2O_5 as the electron-transporting layer for efficient planar perovskite solar cells. *ACS Appl. Mater. Interfaces* **9**, 23181–23188 (2017).
219. Ho Yeon, D., Min Lee, S., Hwa Jo, Y., Moon, J. & Soo Cho, Y. Origin of the enhanced photovoltaic characteristics of PbS thin film solar cells processed at near room temperature. *J. Mater. Chem. A* **2**, 20112–20117 (2014).
220. Kirner, S. et al. Silicon heterojunction solar cells with nanocrystalline silicon oxide emitter: insights into charge carrier transport. *IEEE J. Photovolt.* **5**, 1601–1605 (2015).
221. Biron, R. et al. Window layer with p doped silicon oxide for high V_{oc} thin-film silicon n-i-p solar cells. *J. Appl. Phys.* **110**, 124511 (2011).
222. Hamma, S. & Cabarrocas, P. R. Determination of the mobility gap of microcrystalline silicon and of the band discontinuities at the amorphous/microcrystalline silicon interface using in situ Kelvin probe technique. *Appl. Phys. Lett.* **74**, 3218–3220 (1999).
223. de Vrijer, T., Si, F. T., Tan, H. & Smets, A. H. M. Chemical stability and performance of doped silicon oxide layers for use in thin-film silicon solar cells. *IEEE J. Photovolt.* **9**, 3–11 (2019).
224. Yang, X., Chen, J., Liu, W., Li, F. & Sun, Y. Single-side heterojunction solar cell with microcrystalline silicon oxide emitter and diffused back surface field. *Phys. Status Solidi A* **214**, 1700193 (2017).
225. Spear, W. E. & Le Comber, P. G. Substitutional doping of amorphous silicon. *Solid State Commun.* **88**, 1015–1018 (1993).
226. Tsai, H., Lin, W., Sah, W. J. & Lee, S. The characteristics of amorphous silicon carbide hydrogen alloy. *J. Appl. Phys.* **64**, 1910–1915 (1988).
227. Tawada, Y., Kondo, M., Okamoto, H. & Hamakawa, Y. Hydrogenated amorphous silicon carbide as a window material for high efficiency a-Si solar cells. *Sol. Energy Mater.* **6**, 299–315 (1982).
228. Fell, A. A Free and Fast Three-Dimensional/Two-Dimensional Solar Cell Simulator Featuring Conductive Boundary and Quasi-Neutrality Approximations. *IEEE Trans. Electron Devices* **60**, 733–738 (2013).
229. Feldmann, F. et al. A study on the charge carrier transport of passivating contacts. *IEEE J. Photovolt.* **8**, 1503–1509 (2018).
230. Nogay, G. et al. Interplay of annealing temperature and doping in hole selective rear contacts based on silicon-rich silicon-carbide thin films. *Sol. Energy Mater. Sol. Cells* **173**, 18–24 (2017).
231. Wan, Y. et al. Conductive and stable magnesium oxide electron-selective contacts for efficient silicon solar cells. *Adv. Energy Mater.* **7**, 1601863 (2016).
232. Masmitjà, G. et al. V_2O_x -based hole-selective contacts for c-Si interdigitated back-contacted solar cells. *J. Mater. Chem. A* **5**, 9182–9189 (2017).
233. Wan, Y. et al. Tantalum oxide electron-selective heterocontacts for silicon photovoltaics and photoelectrochemical water reduction. *ACS Energy Lett.* **3**, 125–131 (2018).
234. Tong, H. et al. Dual functional electron-selective contacts based on silicon oxide/magnesium: Tailoring heterointerface band structures while maintaining surface passivation. *Adv. Energy Mater.* **8**, 1702921 (2018).
235. Brendel, R. et al. Breakdown of the efficiency gap to 29% based on experimental input data and modeling. *Prog. Photovolt. Res. Appl.* **24**, 1475–1486 (2016).

Acknowledgements

The work was supported by funding from King Abdullah University of Science and Technology (KAUST) Office of Sponsored Research (OSR) under award no. OSR-CRG URF/1/3383, as well as funding from Saudi Aramco. Figures 2 and 4, as well as the text box images, were created by Heno Hwang, scientific illustrator at KAUST. T.G.A. and J.B. would like to thank prof. Andres Cuevas for guidance and feedback related to the physics of passivating contacts.

Competing interests

The authors declare no competing interests.

Additional information

Supplementary information is available for this paper at https://doi.org/10.1038/s41560-019-0463-6.

Reprints and permissions information is available at www.nature.com/reprints.

Correspondence should be addressed to S.D.